Missouri S&T Library and Learning Resources

Scholars' Mine

Masters Theses

Student Theses and Dissertations

Spring 2019

Microwave detection of surface breaking cracks in metallic structures under heavy corrosion and paint

John Robert Gallion

Follow this and additional works at: https://scholarsmine.mst.edu/masters_theses

 Part of the Electromagnetics and Photonics Commons

Department:

Recommended Citation

Gallion, John Robert, "Microwave detection of surface breaking cracks in metallic structures under heavy corrosion and paint" (2019). *Masters Theses*. 7883.
https://scholarsmine.mst.edu/masters_theses/7883

This thesis is brought to you by Scholars' Mine, a service of the Missouri S&T Library and Learning Resources. This work is protected by U. S. Copyright Law. Unauthorized use including reproduction for redistribution requires the permission of the copyright holder. For more information, please contact scholarsmine@mst.edu.

MICROWAVE DETECTION OF SURFACE BREAKING CRACKS IN METALLIC STRUCTURES UNDER HEAVY CORROSION AND PAINT

by

JOHN ROBERT GALLION

A THESIS

Presented to the Faculty of the Graduate School of the

MISSOURI UNIVERSITY OF SCIENCE AND TECHNOLOGY

In Partial Fulfillment of the Requirements for the Degree

MASTER OF SCIENCE IN ELECTRICAL ENGINEERING

2019

Approved by

Dr. Reza Zoughi, Advisor
Dr. Mohammad Ghasr
Dr. Joseph Newkirk

© 2019

John Robert Gallion

All Rights Reserved

ABSTRACT

We live in the world of “aging infrastructures”. In this environment, critical and heavily utilized infrastructure, i.e. ships, planes, bridges, etc., are operating at or beyond their designed age. Replacement is no longer an option and “retirement for cause” is the current approach to maintenance and replacement. Consequently, there is an ever-increasing demand for efficient and robust nondestructive evaluation (NDE) methods that can determine the physical health of these structures. Large structures, which are primarily made of metals, either steel or aluminum, are susceptible to high-stress cracking and corrosion. Stress-induced cracks in heavily corroded steel, used in bridges, railroads, storage tanks, etc., are extremely difficult to detect. Current methods have limitations that render inspection to take longer either than it should or risk not detecting an existing crack. Microwave signals readily penetrate through dielectric materials such as paint and corrosion byproducts (i.e., rust), while conducting materials (i.e., metals) strongly reflect microwave signals. Therefore, interrogating a metal surface for surface-breaking cracks is readily possible even in the presence of a relatively thick layer of corrosion or paint. Normally, surface-breaking cracks are very small and the perturbations they cause to an irradiating microwave signal are small in amplitude unless the detection is performed very close to the surface. In this thesis, the implementation of a microwave imaging system that utilizes a synthetic aperture radar (SAR) approach to detect surface-breaking cracks in metallic structures under heavy corrosion and corrosion preventive paints is investigated. The resulting SAR images were analyzed and compared to numerical simulations to identify real-world capabilities and theoretical limitations.

ACKNOWLEDGMENTS

This project could not have happened without the guidance and support of many people. My advisor, Dr. Zoughi, has guided and molded my work into a respectable topic that has real-world applications. Dr. Ghasr has also been instrumental in coming up with new ways to look at problems and challenging oneself to trudge their own path. While reliance on others can lead to finished product, true success comes from having the knowledge to figure out solutions with only pertinent guidance. The hands-on side of the work presented here could not have been accomplished without the facilities located at Missouri University of Science and Technology (Missouri S&T). The salt-fog chamber, at the Materials Research Center (MRC) at Missouri S&T, and the microwave imaging hardware from the *amntl* laboratory were critical to the success of the project as well. I also wish to thank the American Society for Nondestructive Testing (ASNT) for the Graduate Fellowship that played an important, positive role in completing and reaching the outcome of this research. Furthermore, the advice and constructive criticisms from my committee fine-tuned the process and increased the impact of the study. Finally, my personal support group, family, and friends, led me on this path just a few short years ago and they have been rooting for me the whole way; my success stems from their belief in me. From a simple “you got this,” to helpful advice, everyone who has been involved has made this project a success.

TABLE OF CONTENTS

Page

LIST OF ILLUSTRATIONS

1. INTRODUCTION

1.1. RATIONALE

Aside from concrete, metals are the most common building materials. Metals provide for significant construction versatility and durability. However, steel and aluminum, which are found in bridges, ships, planes, railroads, etc., are susceptible to corrosion and cracking, as shown in Figure 1.1. To avoid corrosion many of these structures are coated with corrosion-resistant materials or paint. As structures age, the effectiveness of these coatings, to inhibit corrosion, decreases and subsequently potential for stress-corrosion cracking increases. The cost associated with this type of maintenance and rehabilitation is quite high. It has been estimated that, in the US, the total cost of just corrosion related infrastructure maintenance exceeds $140 billion USD annually [1]. Currently there are several standard nondestructive testing methods for detecting cracks in large structures, namely: ultrasonic (UT), eddy current (EC), radiography, dye penetrant and magnetic particle inspection (MPI) testing. Each of these methods have their own advantageous features and limitations. However, as it relates to detecting cracks under heavy corrosion, each significantly suffers from being able to robustly detect hidden cracks. Thus, developing a method to increase crack detection capability and minimize evaluation time and cost is very desirable.

An advantage of using microwave or millimeter wave signals is that they penetrate nonmetallic materials or dielectrics and reflect off conducting materials. This is highly desirous when inspecting structures for cracks that are hidden below a layer of corrosion or in some cases have been painted over after the fracture has occurred. In the

case of a metallic surface covered with paint and corrosion, as shown in Figure 1.2, the microwave or millimeter wave signals penetrate through the layers of dielectrics and reflect from the metals surface. Unique and additional scattered signals from a small defect (i.e. crack) can be detected and imaged through these dielectrics. Not needing to remove corrosion or paints significantly reduces downtime and costs associated with inspections. Currently the Department of Defense (DOD) reports that corrosion related maintenance consumes 25% of the time, about 38 days, that a Navy ship spends in a dry-dock [2]. Decreasing downtime and increasing the probability of detection of critical flaws, especially flaws covered with paint and corrosion has the potential for significant cost and timesaving.

(a) (b)

Figure 1.1: Photos of two severe corrosion cases on painted steel: (a) on an aquatic vessel (source: www.futurecleansystems.com) (b) on a steel railway bridge (source: www.mprnews.org).

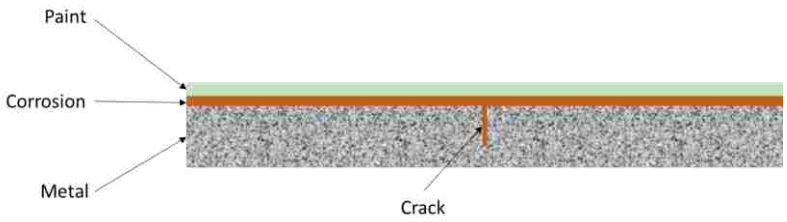

Figure 1.2: Diagram of a crack below corrosion and paint.

1.2. STANDARD NDE METHODS FOR CRACK DETECTION

Currently there are several standard and well-established techniques for detecting surface-breaking cracks in metallic structures. The United States Department of Transportation (US DOT) requires most bridges to be inspected every 24 months [3]. Other than visual inspection, ultrasonic and dye penetrant testing are the main NDE methods when evaluating supporting steel structures for cracks [4]. Eddy current and magnetic particle testing are also used to inspect bridges but because of limitations, their use is usually circumstantial [5]. In aviation, full-scale aircraft known as C or D check inspections occur less frequently than bridges, about every 2 to 6 years [6]. During a D check, the plane is almost entirely disassembled, the paint on the fuselage may even be removed to inspect for cracks and corrosion [6]. The main technique used in inspecting an aircraft fuselage is eddy current, because of its ability to detect surface flaws below a thin layer paint [7]. However, all these methods have limitations that limit their utility for crack detection, which can be overcome using microwave and millimeter wave imaging.

1.2.1. Ultrasonic. Ultrasonic testing (UT) is a well-developed, heavily utilized and standard nondestructive evaluation (NDE) technique. Standard UT testing requires contact between the probe and the structure under inspection while it utilizes high frequency sound waves that scatter or reflect off of flaws [8]. Sound waves, being pressure waves, require that UT techniques have a good physical contact between a UT probe and the object under inspection [8]. Good contact is usually facilitated by a using couplant that must be applied to either the probe or the surface of the material [8]. While UT can be used on a wide variety of materials, including metals and nonmetals, surface roughness or coatings can degrade inspection results [8]. In cases where the structure is

painted or heavily corroded, the effectiveness of UT testing degrades significantly if no surface preparation is implemented.

1.2.2. Eddy Current. Eddy current (EC) inspection is a contact or noncontact electromagnetic NDE method that utilizes changing magnetic fields to induce eddy currents in the material under test [8]. These currents can be disturbed when discontinues or changes in the material occur allowing for detection of any defects on or just below the surface [8]. Because eddy currents can be induced from a distance EC testing is commonly used to find defects below nonconductive coatings as well as the thickness of the coating [8]. This makes aircraft fuselage inspection a very good application for EC testing as cracks and other defects can be detected below a thin layer of paint [7]. However, ferromagnetic materials, such as high iron steels, commonly used in bridges, cause eddy currents to penetrate less deeply, which reduces the sensitivity of the inspection. In addition, the effectiveness of EC testing is also limited by surface variations, coating thickness and changes in standoff distance [8]. Advances in EC testing technology are still in development, multi-probe arrays, other probes are being investigated that improve inspection quality by reducing standoff, and signal saturation (in ferromagnetic metals) related issues [9].

1.2.3. Radiography. Radiographic testing is a noncontact NDE method that utilizes X-ray imaging to detect surface and/or subsurface defects in a variety of materials [8]. Similar to microwave and millimeter wave imaging there is very little sample preparation required for radiography [8]. However, the system preparation (setup and measurement) can be time consuming. Health and safety precautions must be taken when working with ionizing energy, which is the basis of radiography [8]. Field applications

can be difficult or outright impossible, as the evaluation time, and/or safety requirements pose significant limitations compared to other methods [8]. Furthermore, the system cost is much higher than other NDE methods. Disregarding the limitations, radiography has the ability to penetrate through dielectric layers, such as paint or corrosion, to detect smaller cracks than most techniques [8].

1.2.4. Dye Penetrant. Dye penetrant is a chemical-based NDE technique that utilizes a low surface tension liquid to detect small cracks or dimples in a materials surface. While the materials used in dye penetrant testing are low cost, the level of sample preparation varies depending on the structure [8]. When inspecting large structures surface preparation, corrosion and or paint removal, can take a majority of the effort in the operation. Lack of proper surface preparation is the main cause of false indications when conducting dye penetrant testing [8]. In situations where the metal surface is free of surface coatings dye penetrant has been found to reliably, around ~90% of the time, detect cracks down to 3 mm in length [10]. In the field, large structures such as bridges and planes would be very difficult to inspect, especially in cases where heavy corrosion is present.

1.2.5. Magnetic Particle. Magnetic particle (MP) testing is another NDE method, which it utility is limited to ferromagnetic materials. Inspection includes magnetizing the material under test and utilizing small magnetic particles that cluster on the surface of the material and form indications of surface-breaking or shallow defects [8]. Surface and subsurface defects can be detected using this method as both disturb the magnetic fields within the material [8]. As this method magnetizes the part under test it is usually required to demagnetize the part after inspection, which can add to the downtime

of the structure [8]. Like dye penetrant, MP testing works best when the surface is bare and free of debris, and therefore may require pre and post evaluation cleaning, albeit not always [8]. In practice, magnetic particle inspection has been able to detect cracks with a length of 2 mm reliably on bare metallic samples [11]. While this method works on most steels it cannot be used on a nonferrous material such as aluminum.

1.3. MICROWAVE AND MILLIMETER WAVE NDE

Although microwave and millimeter wave inspection are not widely used as NDE techniques they are gaining popularity because of their many versatile and desirable features. The American Society of Nondestructive Testing (ASNT) recently officially recognized microwave and millimeter wave NDE as a testing "Method". The microwave frequency spectrum spans the frequency range of 300 MHz to 30 GHz; while millimeter waves range from 30 GHz to 300 GHz. Materials interact with electromagnetic waves in very specific ways, suitable for many NDE applications [12]. Non-conducting materials, such as dielectrics, can be penetrated by these waves allowing for internal inspection or inspection of multilayered structures. Because of the penetration into dielectrics, material characterization using microwave and millimeter wave NDE can determine the electrical and magnetic properties of materials under test [12]. As material properties are normally unique, especially when considering a large frequency span, changes in material structure or composition can be measured using microwave and millimeter wave NDE. Although microwave and millimeter wave signals penetrate dielectrics, conducting materials such as metals and carbon composites reflect the microwave energy, which limits inspection to

the surface [12]. Depending on the required level of inspection, or the application, different measurement techniques can be utilized.

1.3.1. Previous Work. There are two popular types of microwave and millimeter wave imaging that have been used to detect and image cracks, near-field imaging and Synthetic Aperture RADAR (SAR) imaging. Near-field imaging requires the probe to be very close to the structure being imaged. In the near-field of a probe, the electromagnetic field properties vary substantially as a function of standoff distance and therefore this parameter, like EC testing, must either be known or kept constant during an inspection. However, in near-field imaging or inspection, spatial resolution is a function of probe size and therefore very small defects such as surface-breaking cracks can be detected [13], [14]. Previous research has used near-field millimeter imaging to detect cracks with a width of only 5 μm using a rectangular waveguide operating at ~35 GHz on a bare sample [14]. This research was expanded by repeating the process with a dielectric coating in [13], which showed success using near-field imaging. Other techniques have used circular waveguide probes in [15] and coaxial probes in [16] to accomplish similar tasks using near-field measurements. Additionally, work has been done in [17] – [18] to identify corrosion and pitting under coatings on metal surfaces using near field measurements.

More recently, other imaging methods have dominated new research techniques, allowing for large distances between the probe and target, which can be more desirable in field applications. In one of the commonly used techniques, a relatively large imaging aperture is synthetically produced by moving a probe over the structure under inspection. The collected imaging data in this way is then passed through a SAR algorithm resulting

in high-spatial resolution images of the structure, as shown in Figure 1.3 [19]. Ideally, the maximum resolution obtainable with SAR imaging is λ/4 of the transmitted signal. However, to obtain maximum resolution the size of the synthetic aperture must be large compared to the standoff distance, as shown in Figure 1.4 [19]. For a fixed aperture size, this means as frequency decreases the resolution of the resulting image becomes coarser [19]. Similarly, for a fixed aperture size, the resolution is also a function of standoff distance; this is shown in Figure 1.4. Although using SAR for NDE is a relatively new, SAR imaging has been used for decades for aerial mapping of terrain and remote sensing [20].

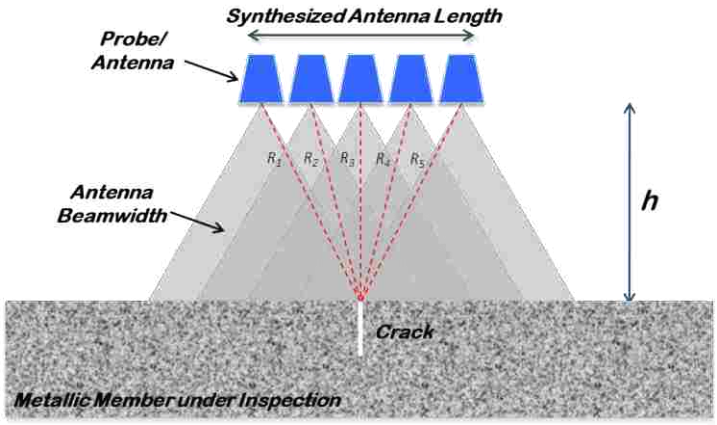

Figure 1.3: Process of generating a synthetic-long imaging aperture.

1.3.2. Preliminary Investigation. Previous research has shown the capability of microwave and millimeter wave NDE to image through dielectric layers in [21] and detect surface breaking cracks in metals in [22]. These ideas were first brought together (imaging a crack through dielectric layers, i.e. corrosion in this case) in [23], which showed that cracks could be successfully identified through corrosion, and simple plane

wave EM simulations corroborated the results found in experimental measurements. While the research [23] proved that imaging cracks through corrosion was possible, the investigation was nowhere near exhaustive. Further tests to determine the limitations of imaging cracks under heavy corrosion and paint on a both steel and aluminum sheets needed to be conducted.

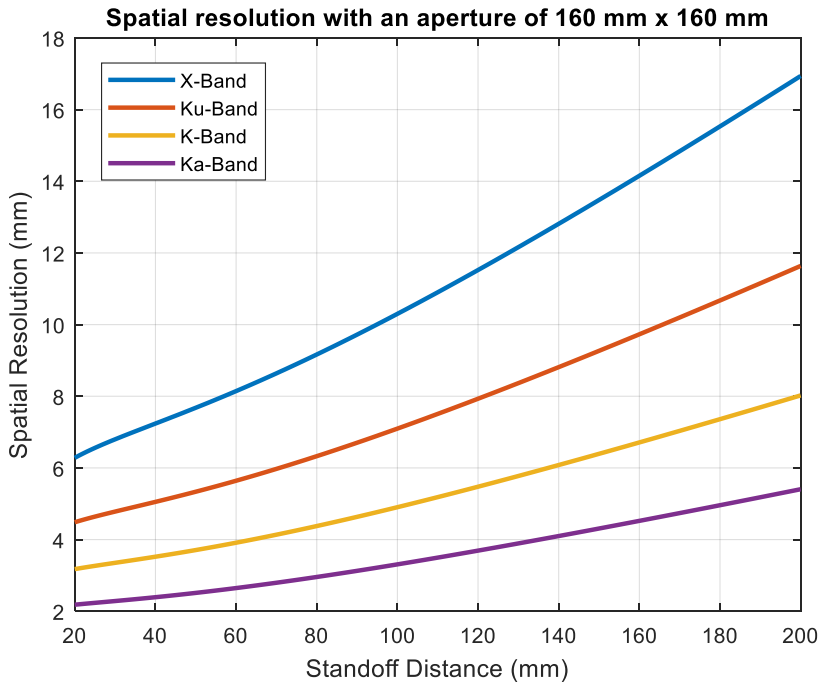

Figure 1.4: SAR spatial resolution based on a fixed synthetic aperture.

1.3.3. Dielectric Properties of Corrosion (Red Rust). In the preliminary investigation the dielectric properties of the corrosion were mostly ignored, that is it was assumed that microwave signals could regularly penetrate the corrosion layer. This assumption was revisited during this investigation to determine the reason behind the disappearing cracks. However, this is not the first study to characterize corrosion.

Dielectric properties of different types of corrosion were thoroughly investigated in [24]. Corrosion similar to that of this study, red rust, was found to have a dielectric constant of ~8.42 – j1.03 [24]. To better characterize the corrosion on the steel samples in this study (which was as combination of corrosion and salt, Fe_2O_3 and NaCl, respectively), material from the surface was removed and characterized using the method described in [25]. The corrosion flakes were gathered from a steel sample after 120 hours in the salt-fog chamber; the flakes were crushed into a powder using a pestle and mortar then filtered with water (to remove excess salt). The relative permittivity and loss factor was calculated at X-band (8.2 – 12.4 GHz) and is shown in Figure 1.5. The corrosion resistant coating, i.e. paint and primer, were made of well characterized materials (polyimide and polyurethane), which have a relatively low permittivity and loss factor.

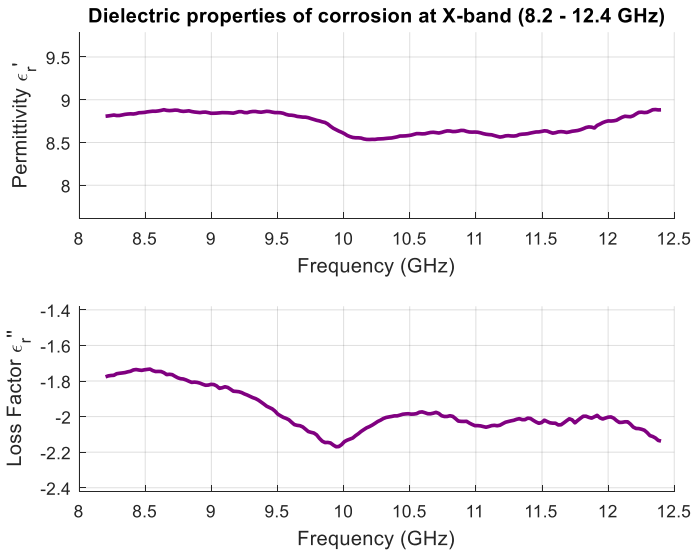

Figure 1.5: Relative permittivity and loss factor of steel corrosion at X-band (8.2 – 12.4 GHz).

1.3.4. Frequency Band Selection. Another aspect that was not investigated in the preliminary investigation, which can be important, is the operational frequency band. As stated before the frequency of the signal used in SAR imaging is very important, as it determines the minimum size of a crack that can be detected. To show this characteristic, images of a test sample were created at X-band (8.2 – 12.4 GHz), Ku-band (12.4 – 18 GHz), K-band (18 – 26.5 GHz) and Ka-band (26.5 – 40 GHz). The test sample included a 6 mm long, 0.3 mm wide EDM (Electrical Discharge Machining) notch located at the center of the 200 mm x 200 mm steel plate, as shown in Figure 1.6. The size of the imaging aperture was kept at 160 mm x 160 mm (smaller than the sample to reduce the edge effects) for all frequency bands, with the probe placed at a fixed standoff distance of 100 mm. The approximate spatial resolution for each of these images can be extracted from Figure 1.4, which was based on the size of these images. The resulting SAR images are shown below in Figure 1.7 (a - d). The crack is only visible at or above Ku-band (12.4 – 18 GHz), with the indication becoming sharper and the crack standing out more from the background with increasing frequency.

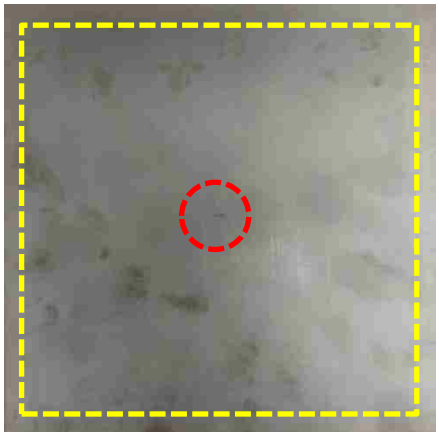

Figure 1.6: Test sample with EDM notch (red), with the superimposed aperture (yellow).

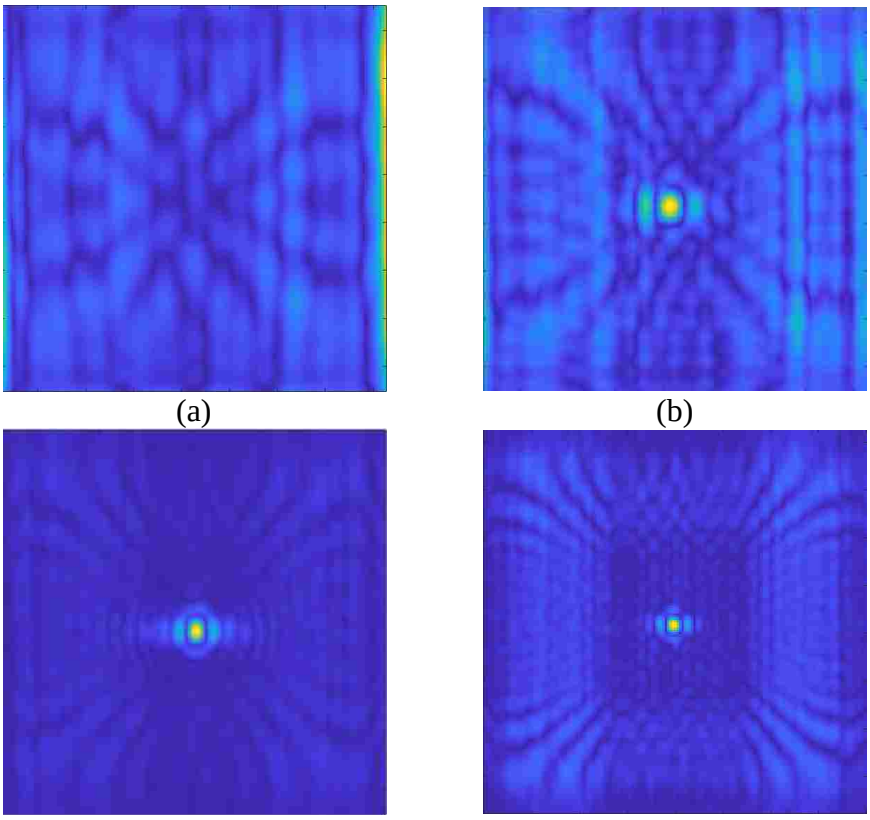

(a) (b)

(c) (d)

Figure 1.7: SAR images of test sample at (a) X-band (8.2 – 12.4 GHz), (b) Ku-band (12.4 – 18 GHz), (c) K-band (18 – 26.5 GHz), and (d) Ka-band (26.5 – 40 GHz)

1.3.5. Polarization. Another consideration when conducting microwave or millimeter wave SAR imaging of cracks is signal polarization. Some objects scatter more signal depending on the polarization of the incident wave. For example, cracks scatter strongly when the polarization of the incoming electric field is orthogonal to the (preferred) length of the crack and almost none when the incoming electric field is parallel to the length of the crack, as shown in Figure 1.8 (a - b). If the surface under inspection is covered with paint or severe corrosion, the orientation of the crack may not be known and could be missed if the orientation falls parallel with the polarization of the incident wave. Two identical (160 mm x 160 mm) SAR images of the test sample were

created using a Ka-band (26.5 – 40 GHz) rectangular waveguide with the polarization orthogonal and parallel to the crack, the resulting images are shown in Figure 1.9 (a) and Figure 1.9 (b), respectively. These results corroborate the results found in plane-wave simulation with the crack being detected when the polarization is orthogonal to the crack. In real-world applications, the crack may not fall completely orthogonal to the polarization of the incoming signal, in these cases the amount of scattered signal is relative to the component of the electric field that is orthogonal to the crack.

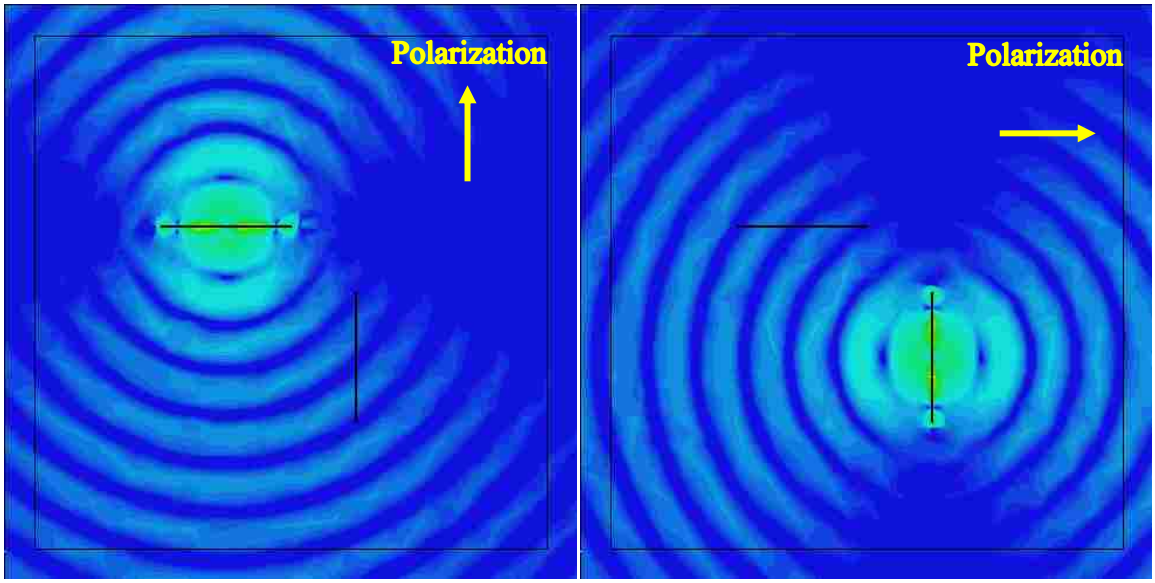

(a) (b)

Figure 1.8: EM simulation of the surface current density from a (a) vertical and a (b) horizontal linear polarized plane wave incident on two orthogonal cracks of length 25.4 mm, width 0.25 mm.

1.3.6. Thesis Work. The research presented in this thesis details the capability of detecting surface breaking cracks on metals using microwave and millimeter wave SAR imaging. Manufactured cracks were made on two types of commonly-used

structural materials, namely: steel and aluminum, which were subjected to induced corrosion in a salt-fog chamber. Samples were either left bare or coated with corrosion resistant paint or primer as they would appear in practical applications. Microwave and millimeter wave SAR images were produced every 24 hours in the salt-fog chamber as the corrosion thickness increased. EM (plane-wave and synthetic aperture imaging) simulations were conducted to corroborate the findings of the experimental measurements. A detection metric, utilizing signal-to-noise Ratio (SNR), was derived and used to determine when a detection was made.

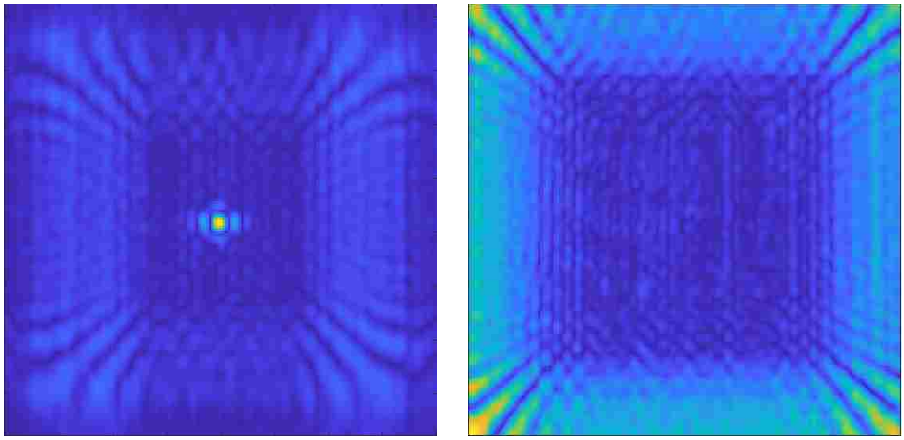

(a) (b)

Figure 1.9: SAR images of the test sample from 100 mm standoff distance with: (a) orthogonal polarization, and (b) parallel polarization.o

2. METHODS

2.1. IMAGING PROCEDURE

To explain how the images were created the details of the system used to gather measurements must first be discussed. Microwave and millimeter wave imaging systems consist of three main components, a probe, a measurement device, and a scanning apparatus. However, in certain situations, such as using a array, the scanning apparatus is not necessary, as many measurements can be made without moving the device.

2.1.1. Probe. Microwave and millimeter wave imaging does not require a certain type of antenna to operate, but certain attributes can be helpful depending on the application at hand. When conducting synthetic aperture radar (SAR) imaging, the antenna must have a relatively wide beamwidth in order to take advantage of the SAR inherent capabilities (i.e., coherent addition of signals from several views). Furthermore, the operation bandwidth determines the range resolution of the SAR image. Incident wave polarization is also an important consideration when determining an appropriate antenna for crack detection applications. Also having the ability to calibrate the antenna is necessary since the SAR algorithm requires a phase reference to properly focus on the structure.

In this study, a linearly polarized open-ended waveguide probe was used, as shown in Figure 2.1a. This probe was selected because it operates within the Ka-band (26.5 – 40 GHz) and the radiation pattern is single sided. Furthermore, standard rectangular waveguides are commercially available at many different frequency bands across the microwave and millimeter wave spectrum. Calibration standards are also well

defined and manufactured for these types of probes, detailed further in [26]. In addition, since the characteristics of the tested cracks were known, determining orientation was not the goal of this work, thus the polarization of the antenna was oriented orthogonal to the sample cracks.

Figure 2.1: Standard linearly polarized open-ended rectangular waveguide probe.

2.1.2. Measurement Devices. In this study, reflective images were created, that is, a signal was sent from a single probe to the crack and the reflected signal that returns to the probe was measured. While other imaging methods exist, this process is quite effective at detecting cracks on metal surfaces, as all signals are reflected at the conductor's surface. These measurements were performed using two types of devices, an Anritsu MS4644A network analyzer (10 MHz – 40 GHz) and an in house wideband millimeter wave interferometer (75 – 110 GHz). Unlike the network analyzer, which can directly measure the magnitude and phase of the reflected signal the interferometer uses a detector that outputs a voltage proportional to the real part of the reflected signal [27]. In either case, the phase referenced data can be processed to make images.

2.1.3. Scanning Procedure. Creating an image requires collecting reflected signal measurements over a given scanning area referred to as the synthetic aperture. This area is scanned at specific step-sizes using a raster scanning platform; a diagram detailing the imaging domain is shown in Figure 2.2. To avoid aliasing in the image step sizes were selected to be smaller than $\lambda/2$ at the highest frequency in the band. Scans were performed with an approximate step size of $\lambda/4$ for the highest frequency of the band, this equates to 2 mm for Ka-band (26.5 - 40 GHz) and 0.75 mm for W-band (75 - 110 GHz). The probes were mounted above the scanning platform so that the samples could be placed on the platform and moved to create the imaging domain. The aperture size, which was kept constant throughout, was (190 mm x 220 mm) for samples 1 and 2, (280 mm x 280 mm) for samples 3 – 5, and (60 mm x 90 mm) for sample 6. To achieve optimal spatial resolution, the standoff distance was kept at 25 mm for Ka-band (26.5 - 40 GHz) and 10 mm for W-band (75 - 110 GHz).

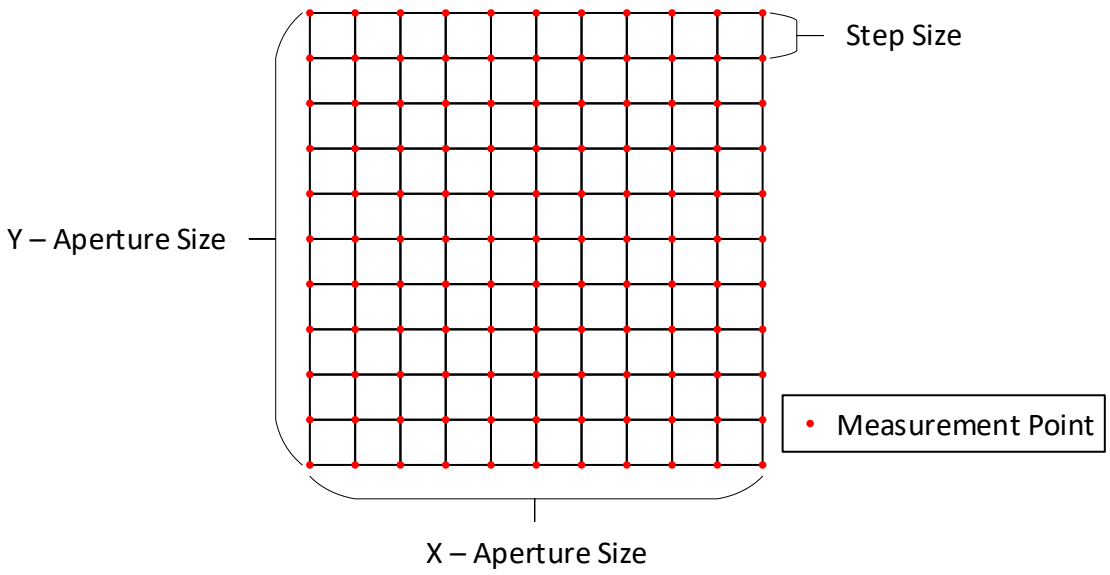

Figure 2.2: Two-dimensional (top down) diagram of a synthetic aperture.

2.1.4. Data Processing. Prior to applying the SAR algorithm, the raw data were resampled, and high pass filtered to remove unwanted artifacts. Artifacts included image features due to changes in standoff distance and "salt and pepper noise" due to fluctuations in the measurement system. "Salt and pepper" noise (i.e. high frequency noise) was more prominent in the W-band system as it was not as stable as the network analyzer. After the data were collected, each image was resampled to twice its original size to reduce image pixilation. After this resampling, each image was passed through a high-pass filter, which removes the effect of standoff distance variation and accentuates the sharp features of a crack. The raw data were then processed using the ω-*k* algorithm and the corresponding 2-D cross-section was used to determine if the crack was detected [19]. Since each image was not taken under the exact same conditions (slight variations in height or calibration quality), each SAR image was normalized to itself. The majority of SAR images are presented in the "jet colormap" which illustrates differences in intensity, red being higher and blue being lower intensities, respectively. Sample 6 however is shown in grayscale as the cracks in the SAR images were more easily detected with a less varying colormap.

2.2. SAMPLE PREPARATION

Two different sets of cracks were created to evaluate the capability of this imaging technique for crack detection. The cracks, in the form of notches, were cut using jeweler saws, into both steel (ASTM A1008) and aluminum (ASTM B209) plates of similar size, ~300 mm x 300 mm with slightly different thicknesses ~2 mm. A steel sample with two fatigue cracks was also included as the "real-world" crack that may be

found on steel bridges. The material types were selected because of their relevance in common infrastructure and susceptibility to corrosion. Before the samples were corroded, the thickness of each was measured at their edges with calipers to determine the starting thickness, so that the corrosion thickness could be measured later. Notches (hereon referred to as cracks) were cut using a 0.15 mm-thick (6 mils) jeweler saw. After the samples were cut, they were lightly sanded to remove sharp burrs and provide a slightly rough surface to promote corrosion. Each sample was then marked with a small hole drilled in the corner to provide an orientation reference as the thickness of corrosion was increased past visual identification.

2.2.1. Crack Layout 1. Crack layout 1 consists of twelve different cracks. Differences in cracks are separated into three regions A, B and C, as shown in Figure 2.3. Region A has four different length cracks ranging from 25.4 mm to 6.35 mm, with an approximate depth of 0.25 mm. The cracks in Region B are identical in length to the cracks in Region A, although the depth of each crack was increased to 0.5 mm. Region C consists of one-inch cracks with a depth of 0.5 mm that are rotated by 0, 15, 30, 45 degrees from left to right, respectively. Sample 1 (steel) and 2 (aluminum) were made with this layout, as shown in Figure 2.4 (a) and (b), respectively.

2.2.2. Crack Layout 2. Crack layout 2 was made to focus on the effects of surface coatings and cracks through the thickness of samples. Layout 2 had only two regions consisting of two cracks each, Region A consisted of cracks that were cut through the sample while Region B consisted of cracks that had a depth of half the thickness of the sample. Two types of corrosion resistant spray paints were obtained, namely; one a paint and primer blend and the other just a primer. These corrosion resistant coatings

were applied (sprayed on) to half of each region so that there was one covered and uncovered cut of each type.

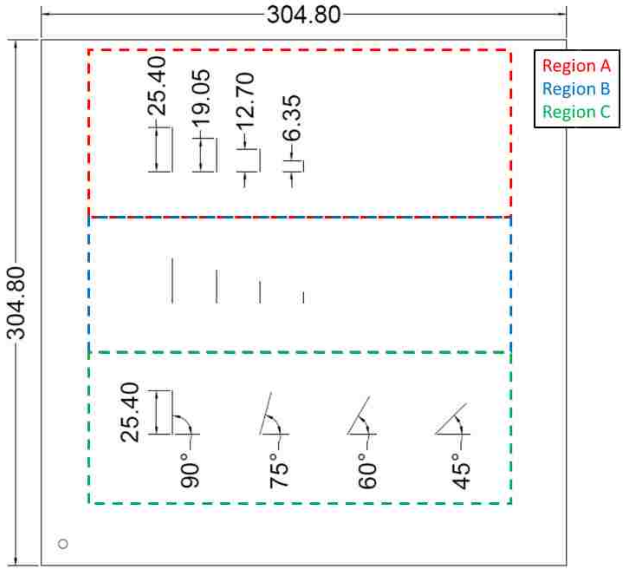

Figure 2.3: Crack layout 1 schematic.

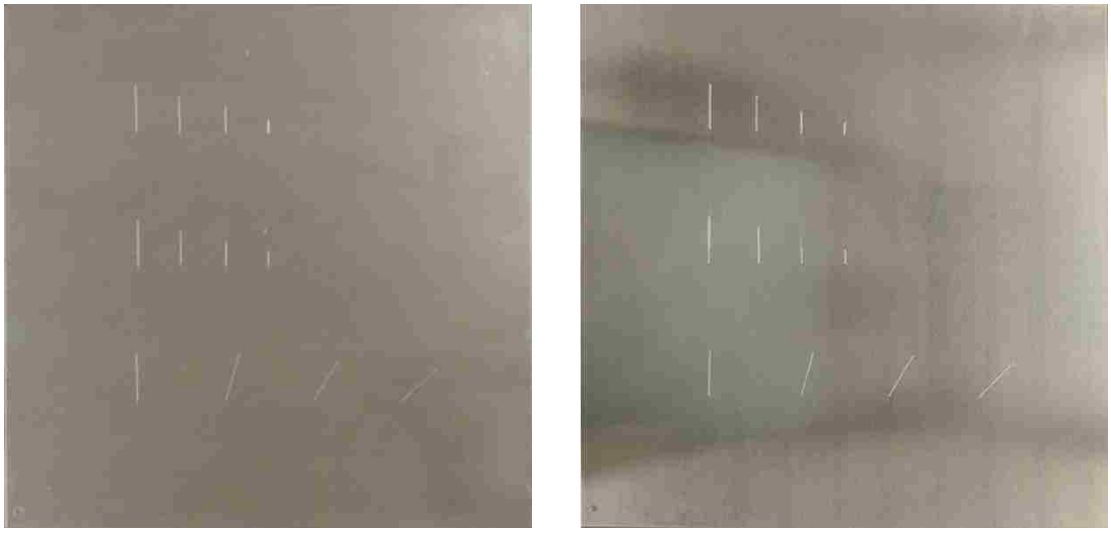

Figure 2.4: (a) Sample 1: steel sample with no coating, and (b) Sample 2: aluminum sample with no coating.

The average coating thickness was ~0.15 mm. Several slashes, through the coating, were made around the painted cracks to facilitate corrosion under the paint, as shown in Figure 2.5. The conventional X pattern was used on the through-crack while orthogonal lines were used on the other crack to reduce scattering. The unpainted side was left bare to compare the differences in measurement capability as a function of surface coatings. Two steel samples and one aluminum sample were made with this layout, as shown in Figure 2.6 (a) – (b) and 2.7, respectively. One steel and aluminum sample were coated with a paint and primer combination. An additional steel sample was coated with only a primer to improve the likelihood of corrosion below the surface.

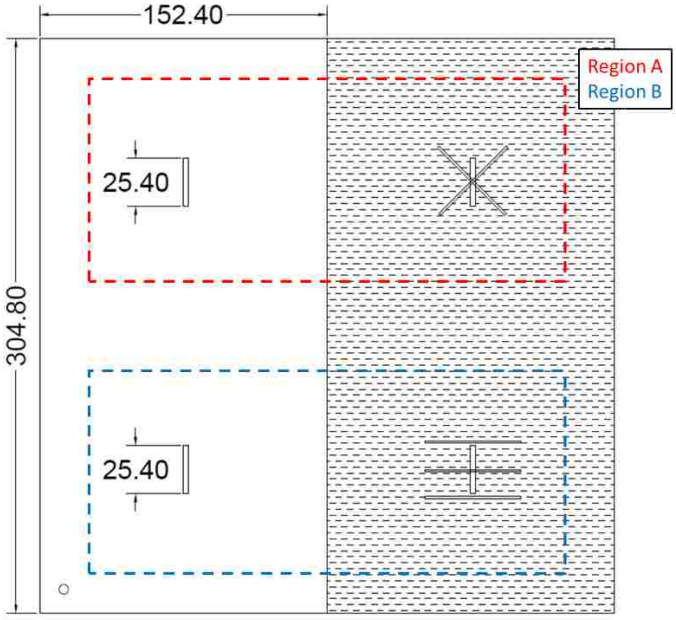

Figure 2.5: Crack layout 2 schematic.

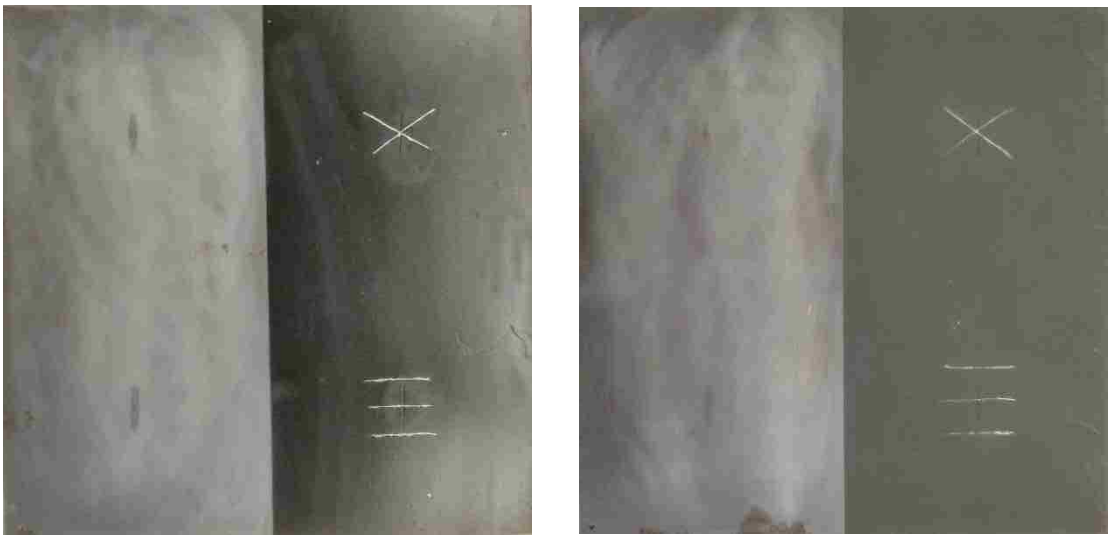

(a) (b)

Figure 2.6: (a) Sample 3: steel sample with paint and primer coating and (b) Sample 4: steel sample with primer coating.

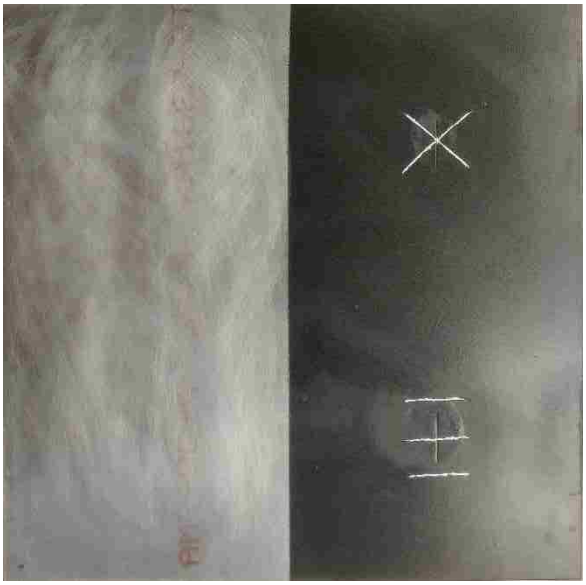

Figure 2.7: Sample 5: aluminum sample with paint and primer coating.

2.2.3. Fatigue Crack. A fatigue crack sample, sample 6, was created prior to the study. The sample is a steel (ASTM A36) plate 300 mm x 120 mm, with a thickness of 12.7 mm, as shown in Figure 2.8. This was originally a part of a “dog bone” sample

that was cyclically fatigued using a closed-loop servo-hydraulic fatigue machine [28]. As the sample was fatigued, cracks also formed around the hole shown in Figure 2.8. Unlike the manufactured cracks, these cracks are true stress fractures, which propagated through the entire thickness of the sample. Although this sample is a real-world crack it is extremely narrow, and in the family of stress-induced fatigue cracks. Consequently, the use of a higher frequency band, W-band (75-110 GHz), was required to detect this crack at distance.

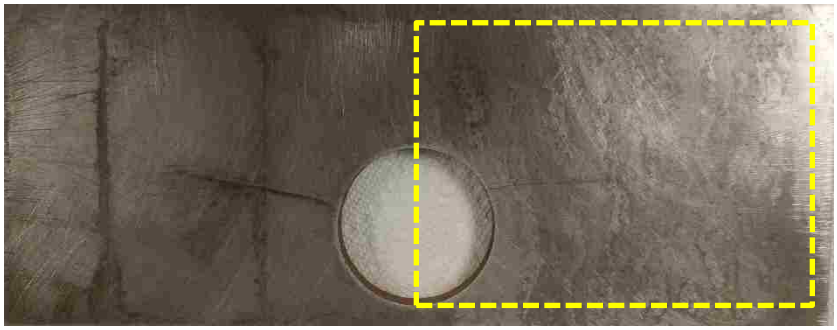

Figure 2.8: Sample 6 steel fatigue crack.

2.3. CORROSION PROCESS

The corrosion process consisted of placing each of the samples in a salt-fog chamber for several 24-hour periods. The salt-fog chamber was a Q-FOG CCT-1100 model, which was large enough to simultaneously house all of the samples so that they were all subjected to identical corrosion-inducing environment. The CCT-1100 also supports a variety of ASTM standards [29]. The ASTM B117 standard was followed in this investigation, which sets the salt concentration, temperature and humidity levels [30]. This standard seemed to work generally well for all samples since the steel samples had

obvious red corrosion after only 24 hours, which built up into thicker layers with longer exposure. The samples were subjected to several 24-hour cycles of corrosion with configuration 1 being subjected for a total of 240 hours and configuration 2 and the fatigue crack for a total of 144 hours. After each interval was completed, the samples were rinsed with deionized water, to remove excess salt on the surface, and were dried over night before being imaged on the scanning tables.

3. IMAGING RESULTS

3.1. SAMPLE 1: SAR IMAGES AT KA-BAND (26.5 – 40 GHZ)

Sample 1 was a bare steel sample with notches as detailed by crack layout 1. A photograph of the sample is shown in Figure 3.1(a) with the approximate scan area superimposed on the photograph. The corresponding 0-hour SAR image, shown in Figure 3.1(b), looks as expected. The relative intensity associated with crack indications (hereon referred to as "intensity") in region A appear lower than the cracks in region B, which have twice the depth. Furthermore, the relative intensity of cracks with identical width and depth is similar, with only the smallest crack indication in region A and B being much fainter than the rest. The relative intensity of the angled cracks also decreases as the angle of the crack and polarization direction become parallel.

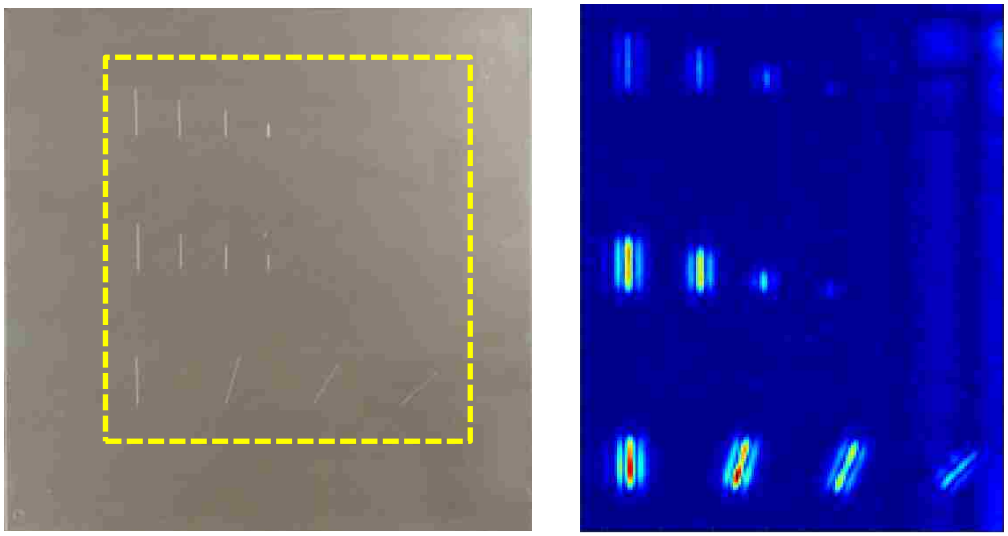

(a) (b)

Figure 3.1: (a) Sample 1 photograph prior to corrosion with marked scan area and (b) SAR image of scan area.

After 24 hours, Figure 3.2 (a), and 48 hours in the salt-fog chamber, Figure 3.2 (b), most of the cracks are still detectable. Once the sample was dried, a caliper was used to note the approximate thickness of the corrosion. Thickness measurements were taken along the edge of the sample and averaged, the apparent change from the 0-hour thickness was assumed to be the corrosion thickness. The corrosion rate of the steel samples averaged ~0.125 mm per 24 hours in the salt-fog chamber but the total thickness varies across the surface of the sample. Surface variation can be seen in the SAR images as slight background noise, which increases in intensity as the amount of corrosion increases. Although corrosion scatters signal at the surface, the amount of signal that is absorbed increases as the thickness of corrosion increases, reducing the amount of signal that reaches the crack. This effect worsens as the thickness of corrosion increases until the crack is no longer detected, which occurs to the cracks in region A and the shortest crack in region B, as shown in Figure 3.2 (a) and (b). Consequently, differentiating these cracks from the background is not readily possible unless one has prior knowledge of these crack locations.

After being in the salt-fog chamber for 72 hours, sample 1 was again photographed. The photograph, which is shown in Figure 3.3(a), shows no visual indications of cracks, as they are covered with a relatively significant layer of corrosion. However, in the SAR image, Figure 3.3(b), ten of the twelve cracks are still detected. The corrosion layer at 72 hours is almost uniform across the sample and was measured to be ~0.4 mm thick. The increase in the background clutter at this stage starts to result in false detections, circled in white in Figure 3.3(b).

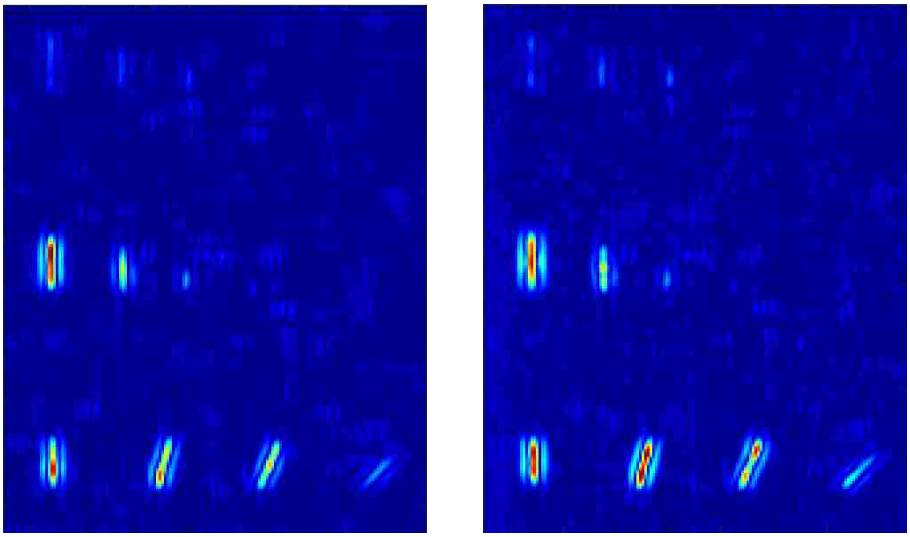

(a) (b)

Figure 3.2: Sample 1 SAR images after (a) 24 hours and (b) 48 hours in the salt-fog chamber.

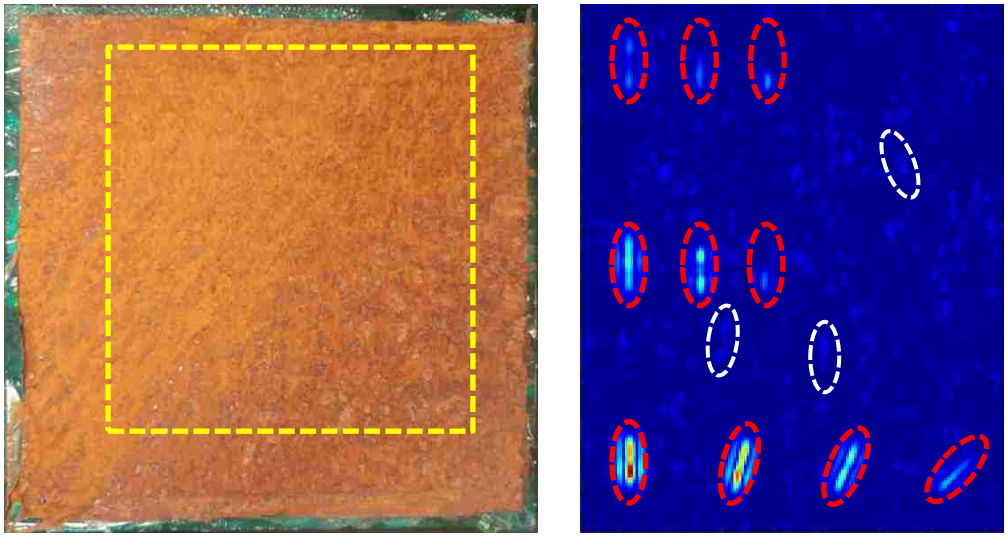

(a) (b)

Figure 3.3: (a) Sample 1 photograph after 72 hours in the salt-fog chamber with marked scan area and (b) SAR image of scan area.

After having been in the salt-fog chamber for 96 hours, the highest intensity, circled in white, is from an area of corrosion, as shown in Figure 3.4 (a). There are also a

few other small indications that are approximately the same intensity as the cracks that are circled in yellow. Nevertheless, at 96 hours, 10 cracks are still detectable in the SAR image. Although after 120 hours in the salt-fog chamber the corresponding SAR image, shown in Figure 3.4 (b), is completely overwhelmed by the intensity of the corrosion and no cracks are detectable. To increase the likelihood of detection the excess corrosion was scraped off and the sample was imaged again, the resulting image is shown in Figure 3.4 (c). Removing the excess corrosion simulates an inspector preparing the surface, or natural flaking of the corrosion off the surface, prior to the measurement. Under heavy corrosion conditions, scraping or otherwise removing excess/loose corrosion may be necessary. After removing the excess corrosion from the sample, as shown in Figure 3.4 (d), all 10 cracks seen in the 96-hour image, Figure 3.4 (a), are visible in the 120-hour image, Figure 3.4 (c).

Following the removal of the excess corrosion at the 120 hours, the sample was corroded again, for an additional 24 hours which puts the total number of hours at 144. Eight cracks were still detected at 144 hours, as shown in Figure 3.5 (a). However, additional corrosion inducement did not result in detecting of any of the cracks, as shown in Figure 3.5 (b - d). As the thickness of corrosion increases, the surface of the sample becomes irregular with areas of thicker corrosion that has built up over time. This shows up in the SAR image as small indications that build up over time, as shown in Figure 3.5 (b-d).

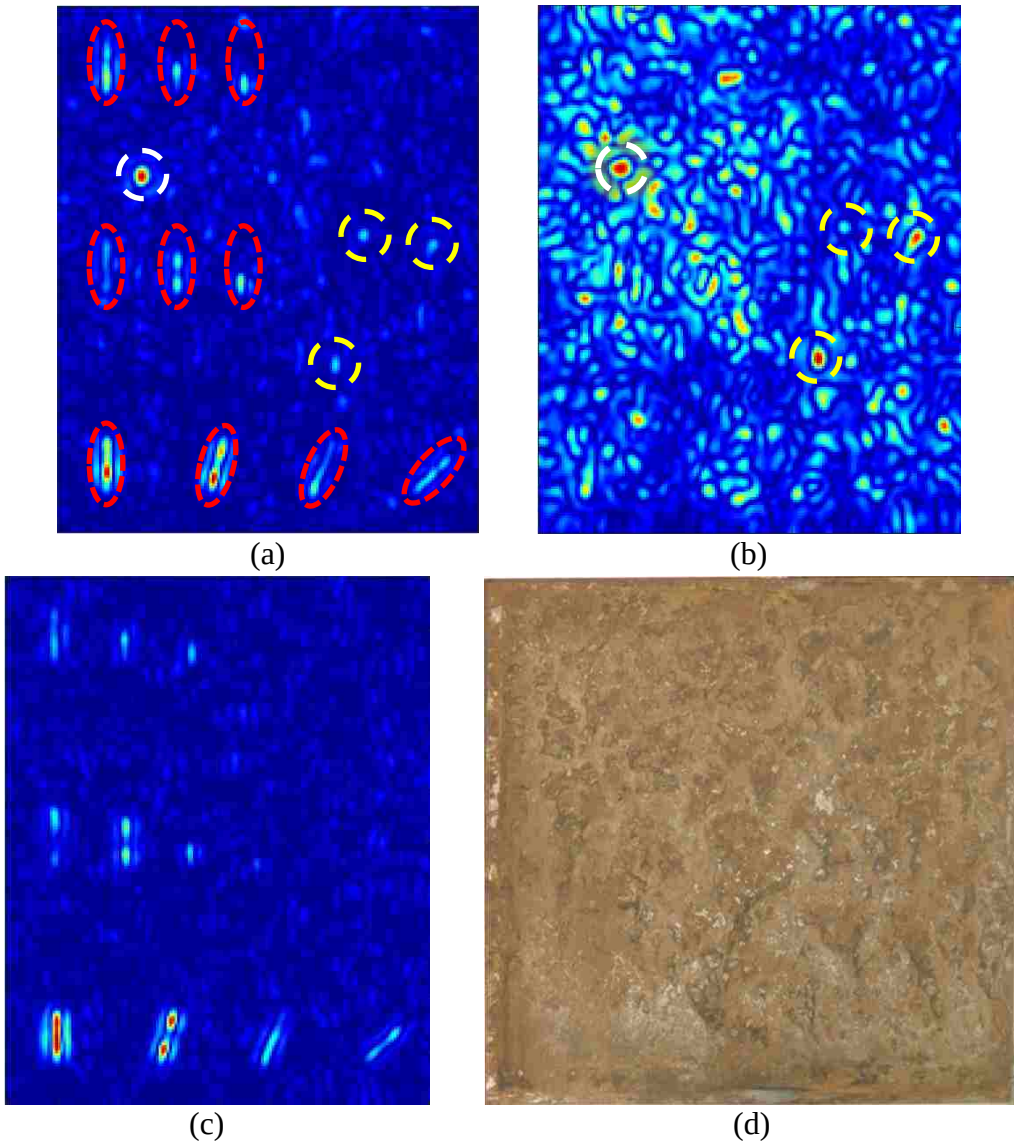

(a) (b)

(c) (d)

Figure 3.4: Sample 1 SAR images after: (a) 96 hours and (b - c) 120 hours in the salt-fog chamber. SAR image (b) before corrosion removal and (c) after corrosion removal.

The final cycle was completed after the sample was in the salt-fog chamber for a total of 240 hours. A picture of the sample can be seen in Figure 3.6 (a) with the original scan area outline. The excess corrosion on the sample was removed again similar to the process done for the 120-hour image. The corresponding SAR image is shown in Figure 3.6 (b). While removing the excess corrosion improves the detection possibility,

highlighted in red in Figure 3.6 (b), the relative intensity is not much higher than the surrounding areas making it difficult to determine if an indication is a crack, especially to an unbiased eye. Figure 3.6 (b) further illustrates that as the amount of corrosion and pitting increases the SAR image becomes more uniform as the magnitude of the returning signal is equal across the entire sample.

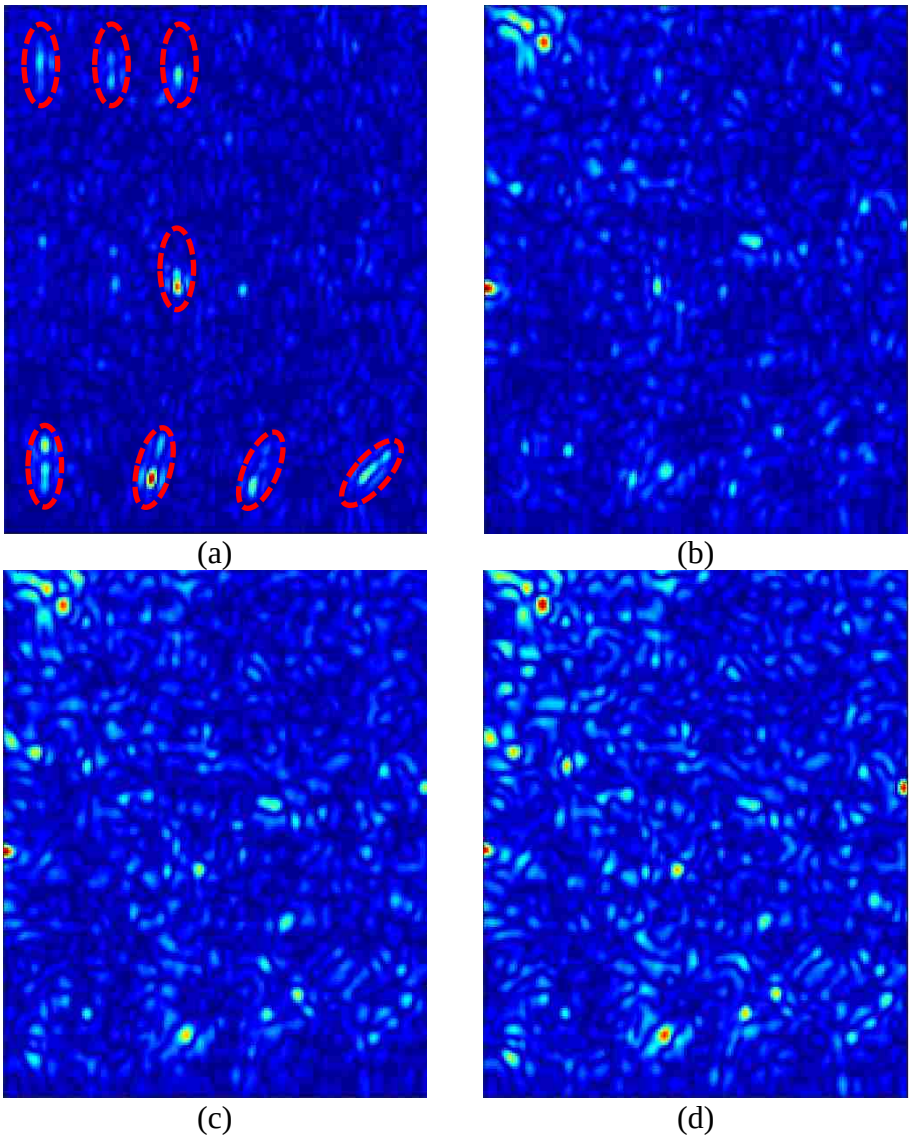

Figure 3.5: Sample 1 SAR images after: (a) 144 hours, (b) 168 hours, (c) 192 hours, and (d) 216 hours in the salt-fog chamber.

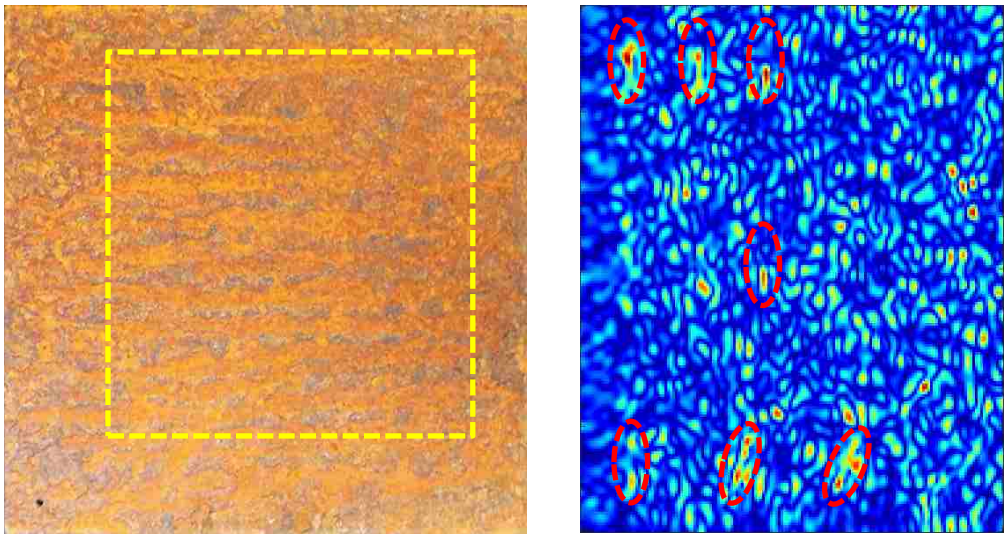

(a) (b)

Figure 3.6: (a) Sample 1 photograph after 240 hours in the salt-fog chamber with marked scan area and (b) SAR image of scan area.

3.2. SAMPLE 2: SAR IMAGES AT KA-BAND (26.5 – 40 GHZ)

Sample 2 is a bare aluminum sample with the notches from crack layout 1, similar to sample 1. A photograph of the sample is shown in Figure 3.7 (a) showing the approximate scan area. The SAR image of the bare sample, as shown in Figure 3.7 (b), shows indications for eight of the twelve cracks, with region A cracks being undetected. Because the cracks were made by hand, the exact depth of the cracks is not known but is approximated. Furthermore, simulations show (in Section 4.2.2) the depth of a crack is related to the relative intensity of the crack, with shallower cracks being less intense as deeper cracks. Therefore, we believe it is likely that these cracks are too shallow to cause a response in the SAR image. In Figure 3.7 (b) the cracks highlighted in red have a distinct region where the response intensity is much stronger than the rest of the crack. The variation along the length of the crack is thought to be due to material left over from the cutting process (burrs). These burrs were only present on the aluminum samples,

which because of the material properties of aluminum, allowed the saw to tear material away from the surface instead of the grinding process that was required to create the cracks on the steel samples. Light sanding prior to imaging could remove these indications but the process was not considered at the time, samples 3-5 were sanded following the creation of the cracks.

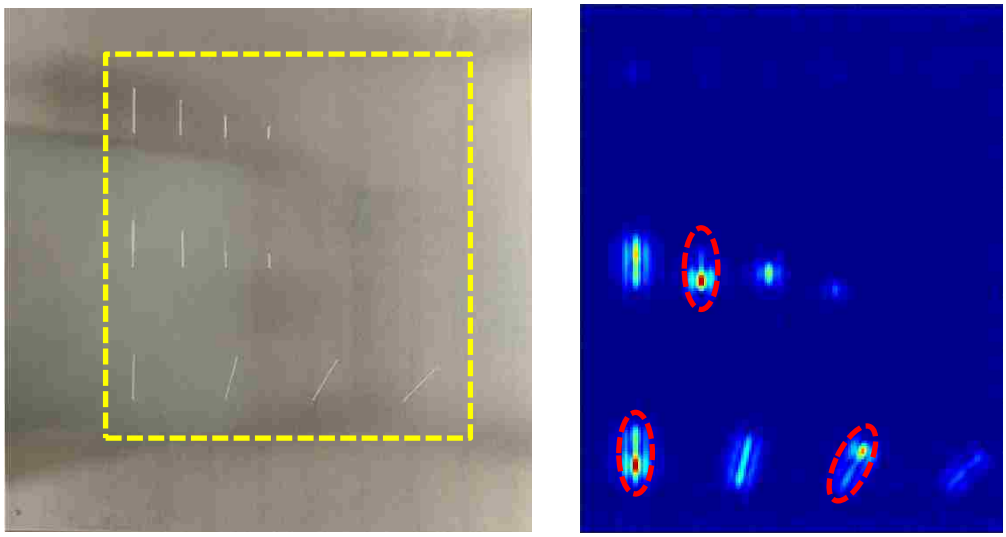

(a) (b)

Figure 3.7: (a) Sample 2 photograph prior to corrosion with marked scan area and (b) SAR image of scan area.

After 24 hours in the salt-fog chamber, the resulting SAR image, shown in Figure 3.8 (a), looks better than the 0-hour image. The overall quality appears improved because the response over the length of each crack is uniform. This leads to an indication that more closely matches a visual representation of a crack. As corrosion forms on the surface, the effect of small physical perturbations (burrs or changes in depth) in the SAR image are reduced. The 48-hour SAR image, which is shown in Figure 3.8 (b), looks

similar overall to the 24-hour image, with only slight changes in the intensity of the cracks.

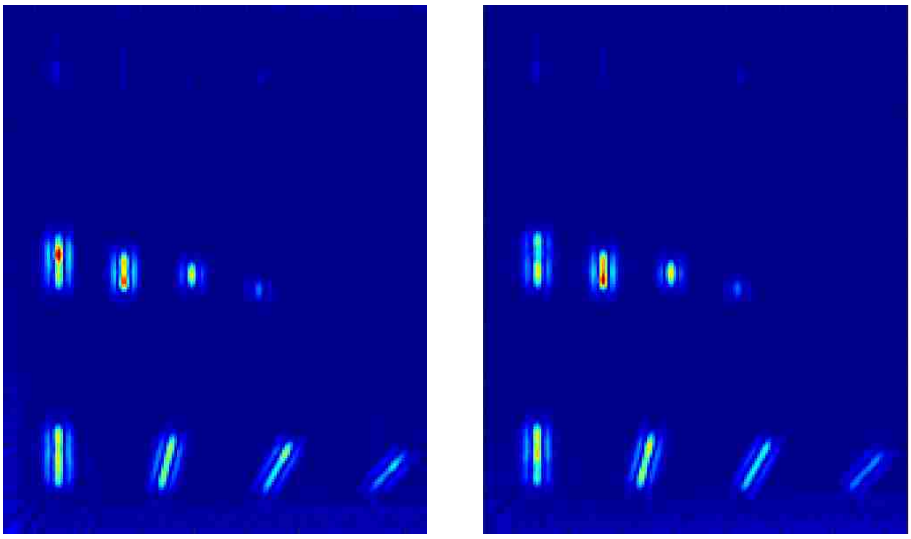

(a) (b)

Figure 3.8: Sample 2 SAR images after (a) 24 hours and (b) 48 hours in the salt-fog chamber.

Unlike sample 1, the aluminum of sample 2 only had a thin layer of corrosion, ~0.1 mm, after being corroded for 72 hours. Figure 3.9 (a) shows a picture of sample 2 after 72 hours in the salt-fog chamber. All twelve cracks can still be (visually) seen on the sample through the light corrosion layer and remaining salt residue (white particles on the sample). In the SAR image, shown in Figure 3.9 (b), the original eight cracks that were detected before the corrosion process are still detectable. The four cracks in region A, outlined in red, are also faintly present but because of the relatively low intensity would be better classified as clutter.

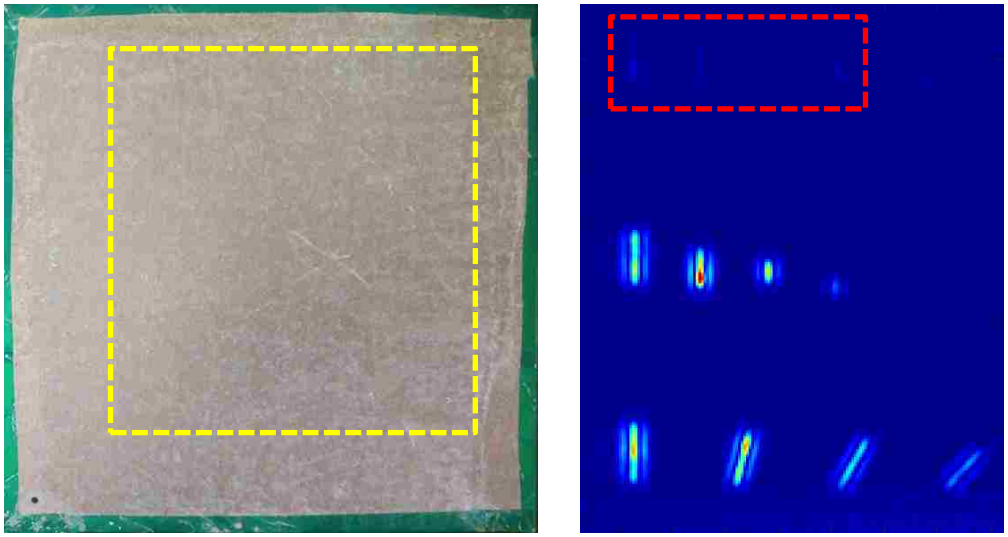

(a) (b)

Figure 3.9: (a) Sample 2 photograph after 72 hours in the salt-fog chamber with marked scan area and (b) SAR image of scan area.

After 72 hours in the salt-fog chamber, each new 24-hour cycle did not result in any considerable difference in the SAR images, as shown in Figures 3.10 (a-f). Aluminum is well known for forming a thin corrosion layer that protects the underlying metal from further corrosion [31]. The majority of the change comes from the increasing thickness of the salt buildup from the solution inside the chamber. The increasing buildup can be seen in the background of the SAR images after the 144 hours in the salt-fog chamber, as shown in Figure 3.10 (c). Although the background intensity increases as the buildup of salt increases it does not overwhelm the response from the cracks, as it did for sample 1.

After a final 24 hours in the salt-fog chamber sample 2 was again photographed, as shown in Figure 3.11 (a). A small amount of red corrosion can be seen on the sample because the samples were accidently stacked before drying.

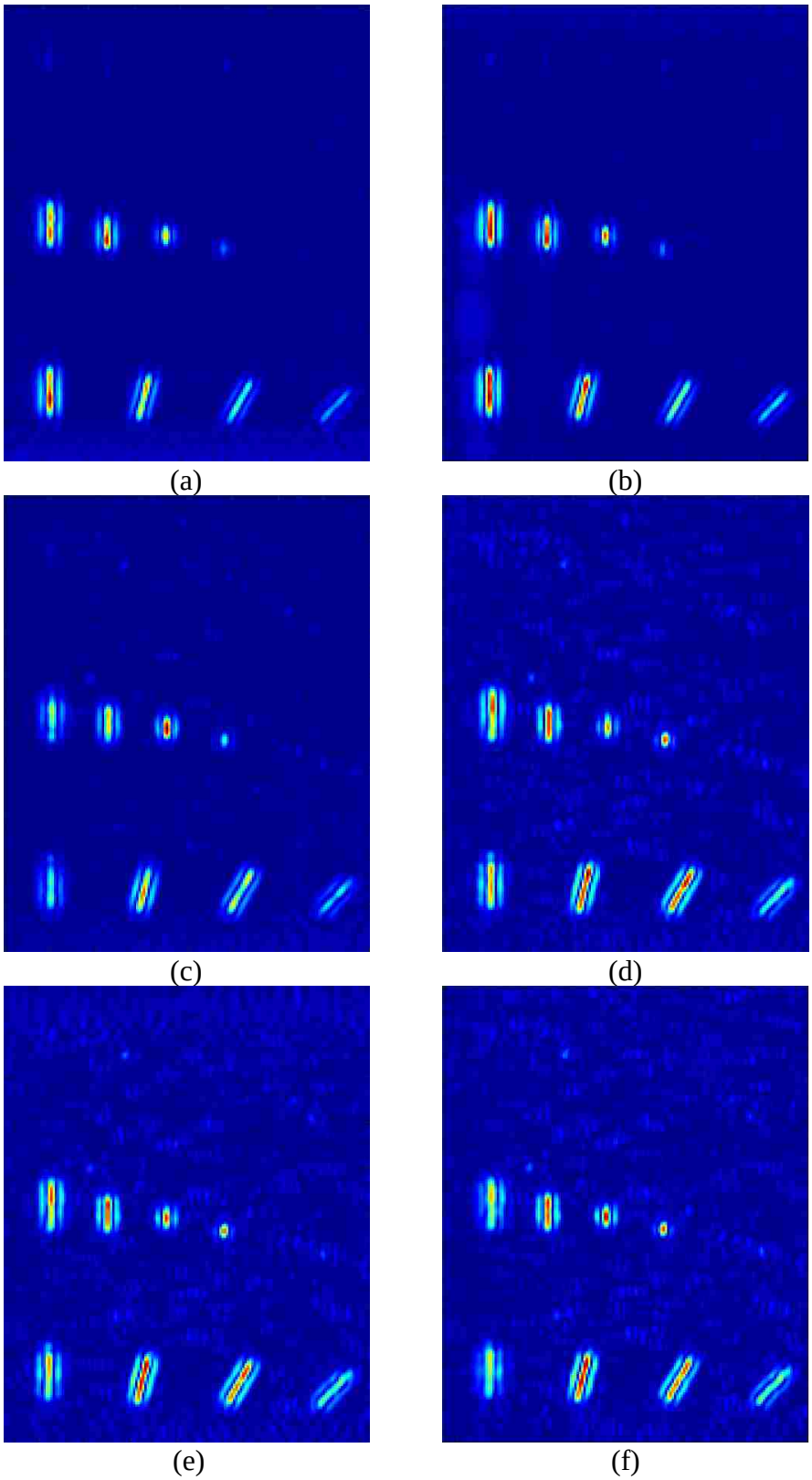

(a) (b) (c) (d) (e) (f)

Figure 3.10: Sample 2 SAR images after (a) 96 hours, (b) 120 hours, (c) 144 hours, (d) 168 hours, (e) 192 hours, and (f) 216 hours in the salt-fog chamber.

However, the amount of additional corrosion is very small, so the effect should be negligible. In preparation for the final scan, sample 2 was thoroughly washed with deionized water to remove as much of the surface salt as possible. The corresponding SAR image with all eight cracks that were detected in the 0-hour image is shown in Figure 3.11 (b). While the indications do not decrease in intensity with size and angle as expected, they are still distinguishable from the background.

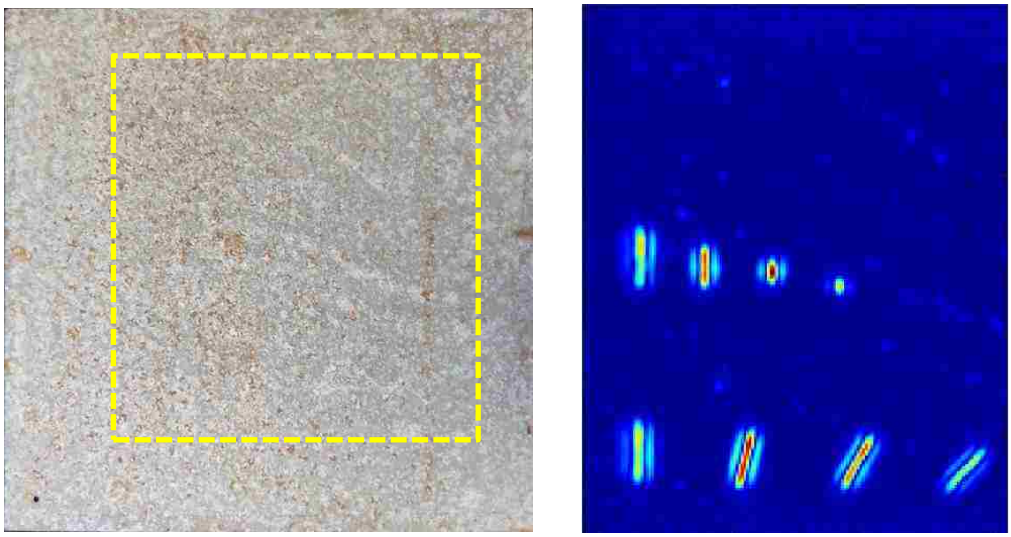

(a) (b)

Figure 3.11: (a) Sample 2 photograph after 240 hours in the salt-fog chamber with marked scan area and (b) SAR image of scan area.

3.3. SAMPLE 3: SAR IMAGES AT KA-BAND (26.5 – 40 GHZ)

Sample 3 was a steel sample with the notches from crack layout 2; it has a paint and primer coating on one-half covering two of the cracks, as shown in Figure 3.12 (a). The 0-hour SAR image, shown in Figure 3.12 (b), shows an indication for each of the four cracks, circled in red. The slashes that were made in the paint to facilitate corrosion

around the cracks are hardly visible in the SAR image because they do not scatter very much signal. The intensity from each crack, especially those in region A, which were through cracks, varies along the length of the crack. This is due to the large radius of circular saw; which is only able to penetrate through the sample at the center of the crack, while keeping the crack on the front of the sample a certain length. The change in depth along the length of the crack causes the intensity of the crack indication to be higher in center of the crack.

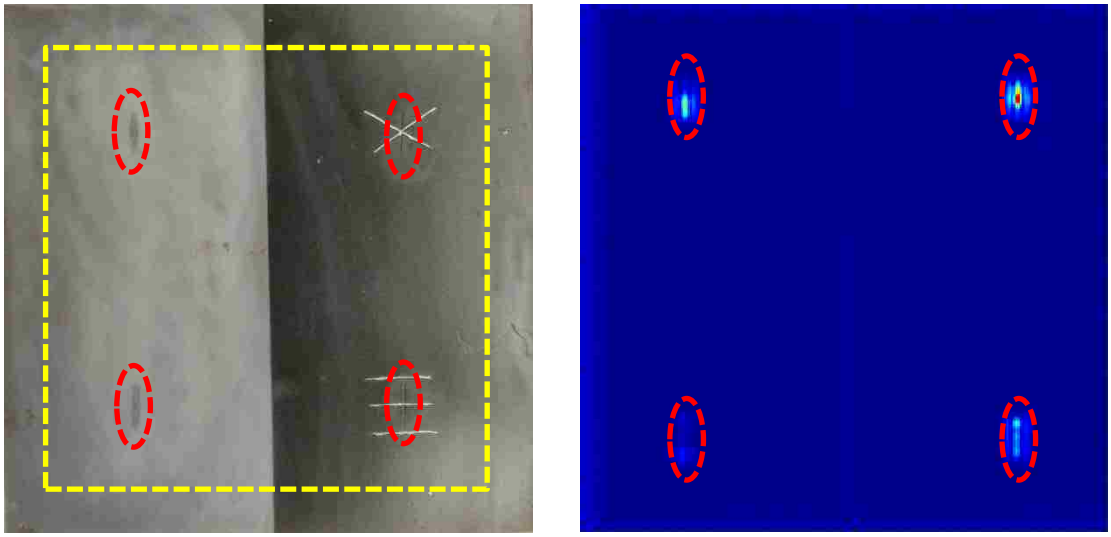

(a) (b)

Figure 3.12: (a) Sample 3 photograph prior to corrosion with marked scan area and (b) SAR image of scan area.

After 24 hours in the salt-fog chamber, the sample was imaged again. However, the scan step size was increased to reduce overall scan time. Increasing the distance between sampling can also reduce the spatial resolution and can cause aliasing if the spacing is too large [19]. These effects can be seen in Figure 3.13 (a) as the background

on the right, the painted side (on the right), shows some variations in image intensity that are not present in either Figure 3.12 (b) or Figure 3.13 (b). After the 24-hour scan the original 2 mm sampling was used throughout all the measurements as the sacrifice in resolution did not outweigh the reduced measurement time. Unlike sample 1, which was also steel, the first 25.4 mm long crack to become undetectable occurred after 48 hours in the salt-fog chamber instead of after 72 hours. The cracks on the bare side of the sample have faded into the background with only part of the crack in region A, highlighted in red, being distinguished. However, since the background has several new indications that could be classified as cracks the indication from region A could be misconstrued as surface variation or otherwise.

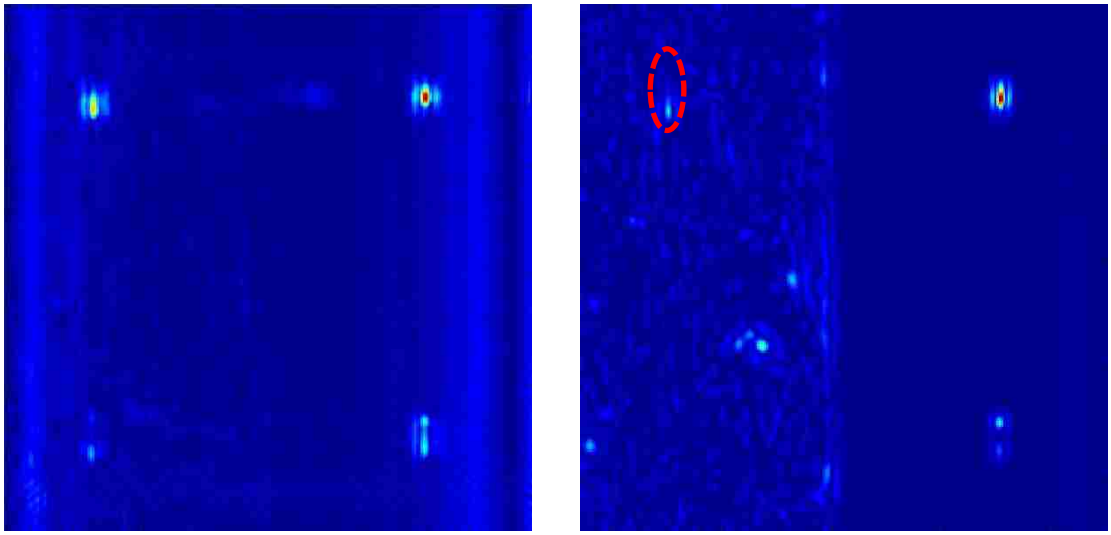

(a) (b)

Figure 3.13: Sample 3 SAR image after (a) 24 hours and (b) 48 hours in the salt-fog chamber.

Figure 3.14 (a) shows the SAR image after the sample was in the salt-fog chamber for 72 hours. Neither of the bare cracks are visually detectable at this time. The

corrosion is quite severe that it is beginning to form at the edges of the painted half of the sample. However, not much corrosion has penetrated the center of the protective layer and the cracks are still visible and are detected in the SAR image, as shown Figure 3.14 (b). As the relative intensity of the corroded side of the sample increases, it begins to overwhelm the response from the cracks. This is the reason the crack in Figure 3.14 (b), highlighted in red, seems to disappear without additional corrosion around the crack. Improving the contrast between the crack and the background, in this case by cropping the corrosion out of the image, improves the likelihood that the crack will be detected during inspection.

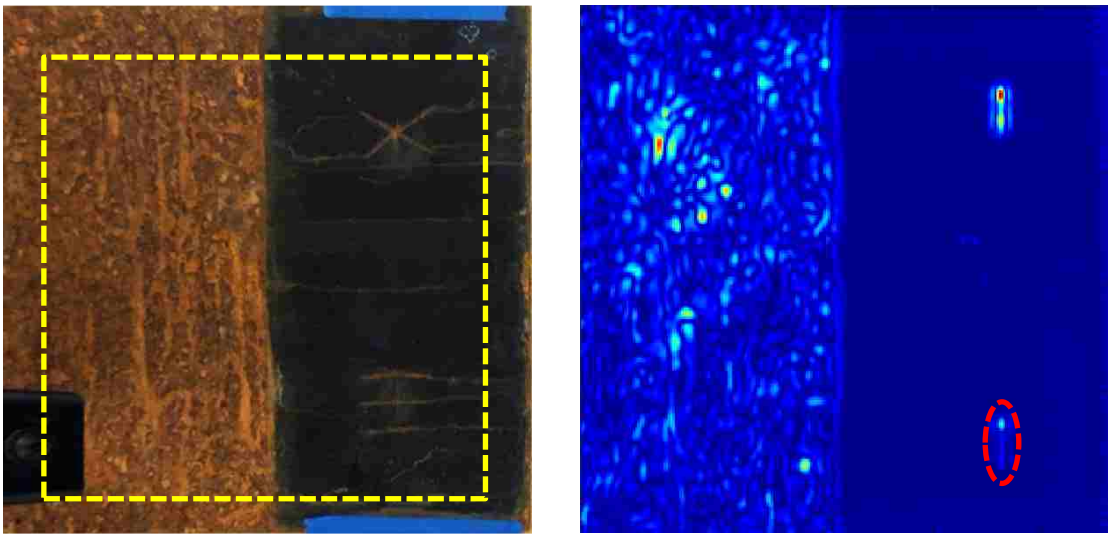

(a) (b)

Figure 3.14: (a) Sample 3 photograph after 72 hours in the salt-fog chamber with marked scan area and (b) SAR image of scan area.

After 72 hours in the salt-fog chamber, the corroded side of the sample started to dominate the features in the image. Therefore, to remove this effect the corroded half was

removed from the following images. At 96 hours in the salt-fog chamber, the slashes that were made on painted side are more prominent and can be seen in the SAR image, as shown in Figure 3.15 (a). The 120-hour SAR image, shown in Figure 3.15 (b), shows similar results, with the region A cracks having higher intensities than those in region B. The overall background has remained mostly unchanged on the painted side, since not much corrosion penetrated the protective layers.

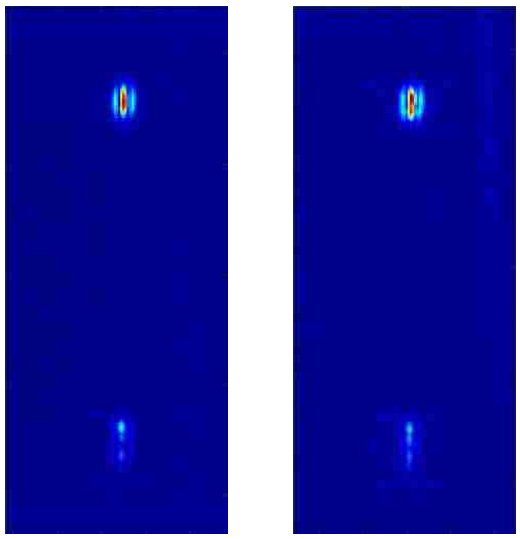

(a) (b)

Figure 3.15: Sample 3 SAR image after (a) 96 hours and (b) 120 hours in the salt-fog chamber.

After 144 hours in the salt-fog chamber the sample was photographed, as shown in Figure 3.16 (a), and imaged, as shown in Figure 3.16 (b), for the final time. The average corrosion thickness on the bare side of the sample was measured to be ~0.9 mm. Furthermore, the paint and primer coating around the edge of the sample has begun to peel off from the corrosion underneath. The slashes that were made over the cracks on the painted side have corrosion that protrudes out further than the protective coating. While

the cracks on the unpainted side are no longer detectable, the cracks on the protected side are still visible in the SAR image, as shown in Figure 3.16 (b).

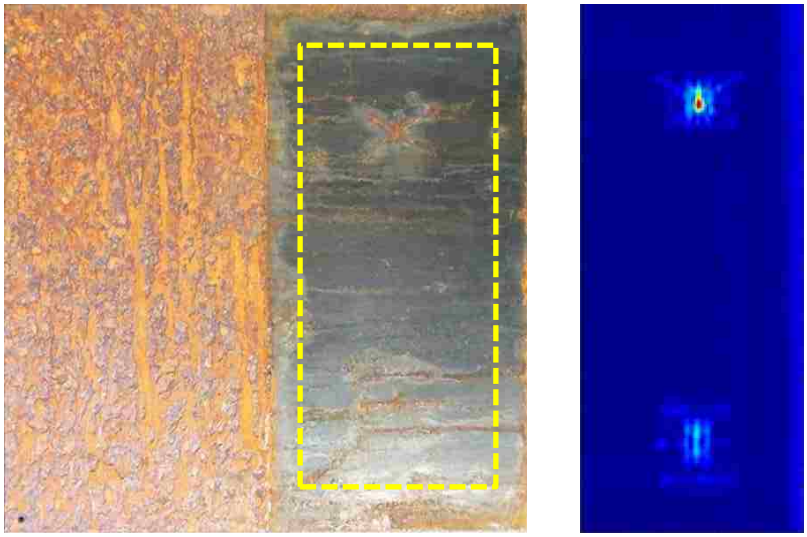

(a) (b)

Figure 3.16: (a) Sample 3 photograph after 144 hours in the salt-fog chamber with marked scan area and (b) SAR image of scan area.

3.4. SAMPLE 4: SAR IMAGES AT KA-BAND (26.5 – 40 GHZ)

Sample 4 was another steel sample, similar to sample 3, however the coating on one half was a corrosion resistant primer instead of the paint and primer mixture, as shown in Figure 3.17 (a). Similar to samples 3 and 5, slashes were made to facilitate corrosion around the cracks that were beneath the coating. Unlike the paint coating, the primer coating did not flake off when scratching the surface, so each slash is made of a few scratches to expose bare metal. In the 0-hour SAR image all four cracks were detected, as shown in Figure 3.17 (b), as well as the border of the protective coating.

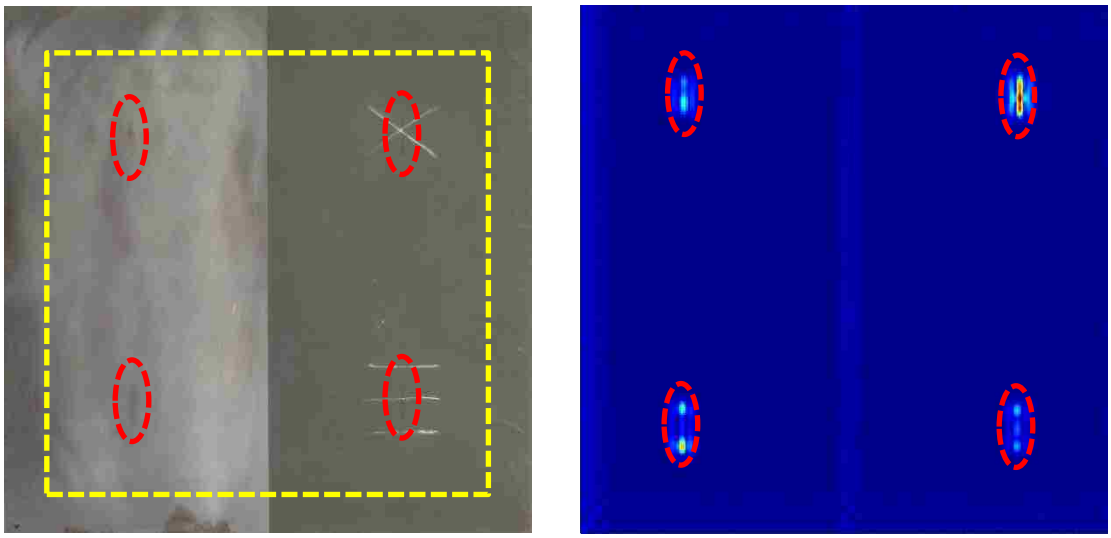

(a) (b)

Figure 3.17: (a) Sample 4 photograph prior to corrosion with marked scan area and (b) SAR image of scan area.

The 24-hour and 48-hour SAR images are very similar to the sample 3 images at the same amount of time in the salt-fog chamber. The 24-hour SAR image, shown in Figure 3.18 (a), appears to have much more background variation, especially on the primed half, compared to the 0-hour and 48-hour images. This variation is due to the increase in scan step size, from 2 mm to 3 mm, between measurement points, which causes a decrease in image quality. The scan step size was initially increased to save time but adversely effected the SAR images. Although the additional step size reduced the quality of the image the cracks were still detectable, and the scans were not redone. Unlike the 48-hour SAR image of sample 3, where only three cracks were detectable (region A crack on the bare side and both cracks on the painted side), all four cracks on sample 4 are still detectable, as shown in Figure 3.18 (b). Slight differences, in depth and width of the cracks, as well as the variation in the thickness of the corrosion are the most likely reasons that all four cracks are still detectable at this time.

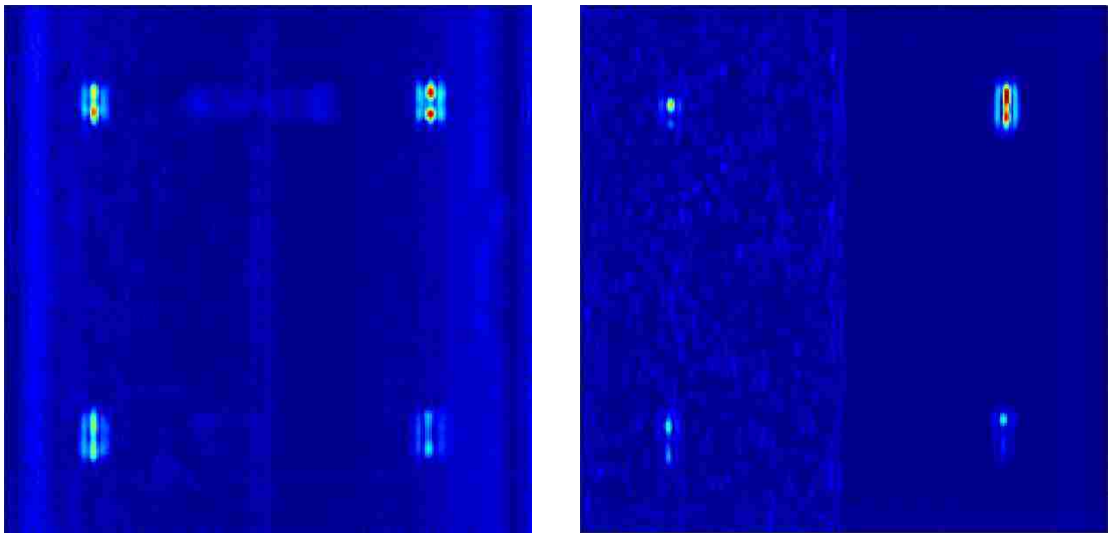

(a) (b)

Figure 3.18: Sample 4 SAR image after (a) 24 hours and (b) 48 hours in the salt-fog chamber.

After 72 hours in the salt-fog chamber, the sample was again photographed, as shown in Figure 3.19 (a). Corrosion not only covers the bare side of the sample but also where the slashes were made. The corrosion at this point is almost uniform with a measured thickness of ~0.375 mm. Figure 3.19 (b) is the last time a crack on the bare side of the sample is detectable. The crack from region A is circled in red in Figure 3.19 (b) based on its known location. However, because the indication is similar in intensity to surrounding clutter the indication could easily be characterized as surface variation. Unlike sample 3 that was coated with paint and primer, the corrosion on the primed side was much less severe along the edges. As expected, the cracks that were coated with corrosion resistive primer are both present, and there is little variation in the intensity of the SAR image for primed portion. The primer layer is however very susceptible to scratching, a small scratch from a bump with another sample is circled in red in Figure 3.19 (a). Small scratches in the protective coating lead to additional image variations that

could eventually mask a crack indication. However, these indications could also be used to detect and repair the protective coating depending on the application.

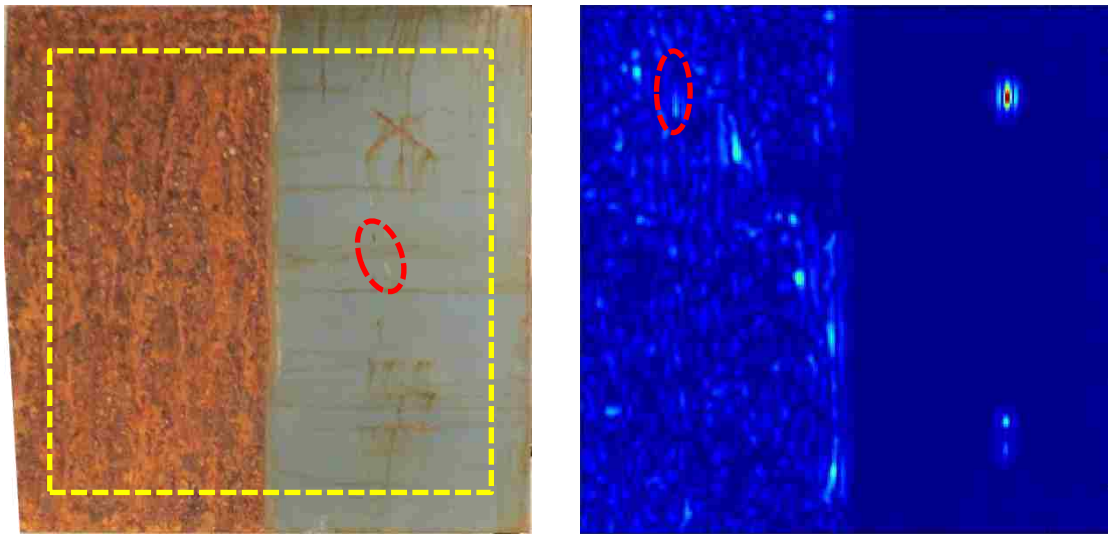

(a) (b)

Figure 3.19: (a) Sample 4 photograph after 72 hours in the salt-fog chamber with marked scan area and (b) SAR image of scan area.

After 96 hours in the salt-fog chamber, the cracks on the bare side of the sample are completely obscured by corrosion. The SAR images have been cropped to improve the visibility of the cracks below the protective coating. Figure 3.20 (a) and (b) show the SAR images for 96 and 120 hours in the salt-fog chamber, respectively. Both cracks are clearly visible in both images. However, the corrosion in the slashes is more prominent and there is additional image clutter after 120 hours in the salt-fog chamber. This clutter, which appears as additional lines in the image, is thought to be due to an imperfect calibration or loose connection throughout the scan as the background variation reduces after additional time in the salt-fog chamber.

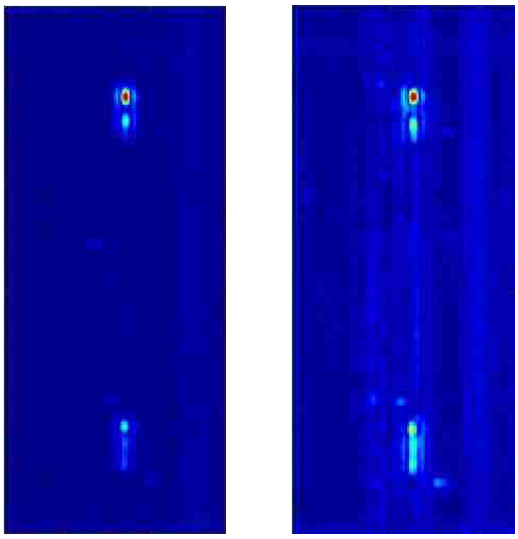

(a) (b)

Figure 3.20: Sample 4 SAR image after (a) 96 hours and (b) 120 hours in the salt-fog chamber.

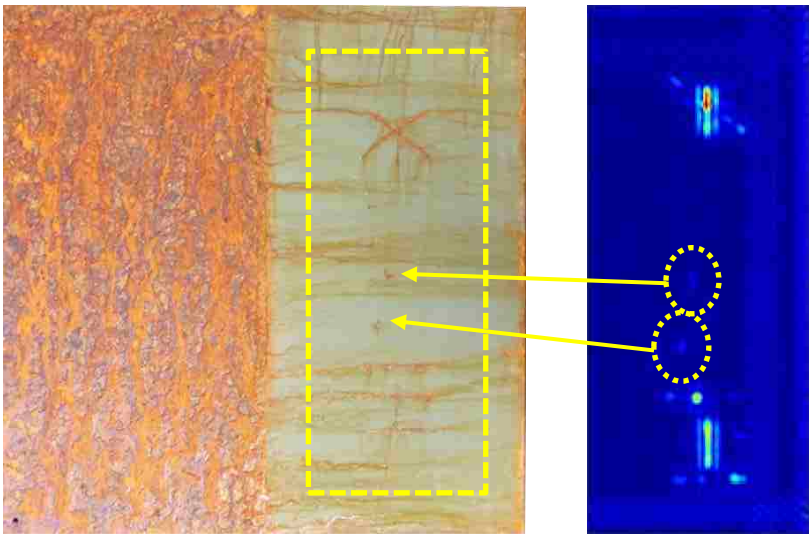

(a) (b)

Figure 3.21: (a) Sample 4 photograph after 144 hours in the salt-fog chamber with marked scan area and (b) SAR image of scan area.

The final SAR image was taken after the sample was 144 hours in the salt-fog chamber. The photograph of the sample and the approximate scan area is outlined in Figure 3.21 (a). The total corrosion thickness at 144 hours was measured to be ~0.9 mm.

The increase in thickness is evident in the SAR image shown in Figure 3.21 (b) as the slashes are clearly visible around the cracks. The small scratches that were accidently made in the primer coating also begin to show more clearly in the SAR image as the amount of corrosion from those areas exposed increases, as highlighted in Figure 3.21 (b). However, the overall background intensity is still much lower than the intensity of the cracks, allowing for easy detection.

3.5. SAMPLE 5: SAR IMAGES AT KA-BAND (26.5 – 40 GHZ)

Figure 3.22 (a) is a photograph of sample 5, which was an aluminum sample with notches outlined in crack layout 2 along with a paint and primer coating on one half. The corresponding 0-hour SAR image, shown in Figure 3.22 (b), shows an indication for each of the four cracks, highlighted in red. Similar to samples 3 and 4, the cracks in region A appear much shorter than the actual length of the crack due to the size and shape of the saw that was used. Although the through cracks on the aluminum sample seem to reflect strongly, the notches that make up region B have much lower intensity and are more difficult to distinguish.

The SAR images for hours 24 and 48 in the salt-fog chamber are shown below in Figures 3.23 (a) and (b) respectively. Similar to previous 24-hour images, Figure 3.23 (a) shows the reduction of image quality as the scan step size is increased, from 2 mm to 3 mm. As the intensity of the background increases, crack indications in a properly focused image will be more easily detected. After the 24-hour image the scan step size was returned to 2 mm for the following images. While the sample in Figure 3.23 (b) (48 hours) has undergone 24 more hours in the salt-fog chamber than Figure 3.23 (a) (24

hours) the intensity associated with the crack is much higher than the background intensity and its variations.

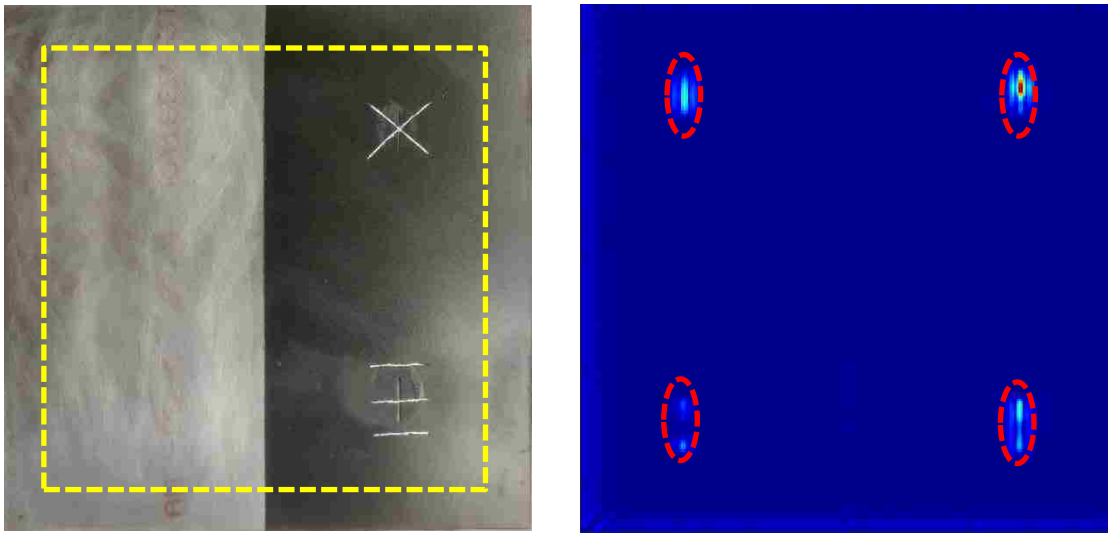

(a) (b)

Figure 3.22: (a) Sample 5 photograph prior to corrosion with marked scan area and (b) SAR image of scan area.

After 72 hours in the salt-fog chamber, the sample was photographed again, as shown in Figure 3.24 (a). Similar to sample 2 the thickness of corrosion did not seem to increase very much as a result of the additional 24 hours. At 72 hours, the total thickness of corrosion and salt byproducts was only ~0.1 mm. If the sample was not thoroughly rinsed, the salt layer would continue to build up as a function of increase in the exposure time in the chamber. In real world applications, seafaring vessels may have this layer prior to cleaning. The corresponding SAR image, shown in Figure 3.24 (b), shows a more prominent corrosion/salt layer is more prominent and has begun to form around the

slashes. However, the image intensity associated with the corrosion is low compared to the intensity of the cracks, which are all detected in the image.

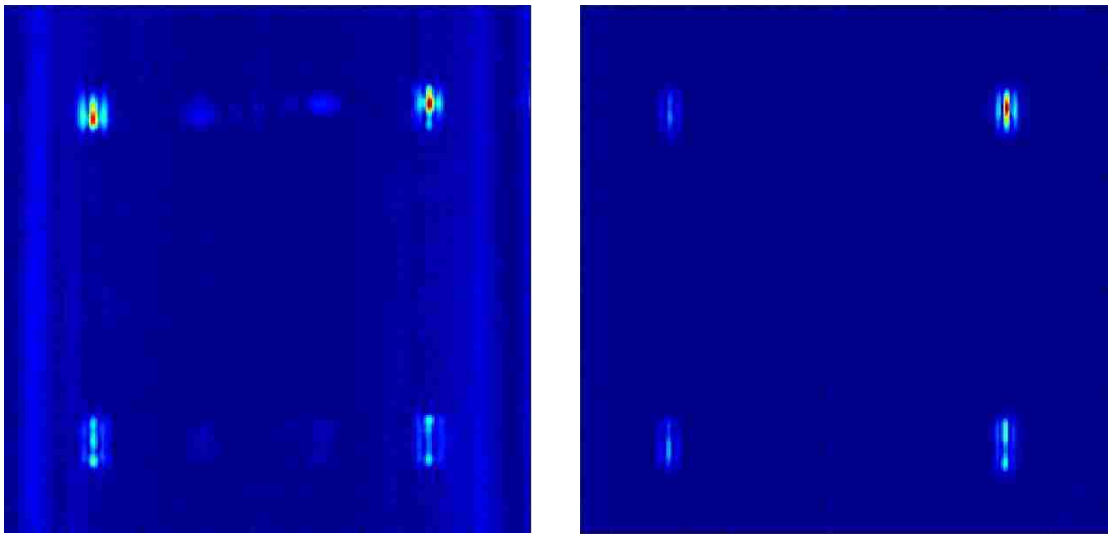

(a) (b)

Figure 3.23: Sample 5 SAR image after (a) 24 hours and (b) 48 hours in the salt-fog chamber.

After 72 hours in the salt-fog chamber, the sample was no longer cleaned after each interval to allow the salt layer to increase in thickness to provide an example of imaging through a non-uniform low permittivity coating. The increase in background intensity due to the additional thickness of the salt layer can be seen in Figures 2.35 (a) and (b). Unlike the steel samples that had little to no corrosion spread under the paint around the slashes, sample 5 had significant bubbling of the paint around the slashes and near the edge of the coating, examples of which are circled on Figure 3.25 (b). This bubbling increases the variation of the background intensity around each of the cracks on the painted side of the sample. Although aluminum oxide seems to form below the

corrosion resistant coating, the relative intensity of the corrosion is low enough that the cracks may still be detectable after the coating has worn away.

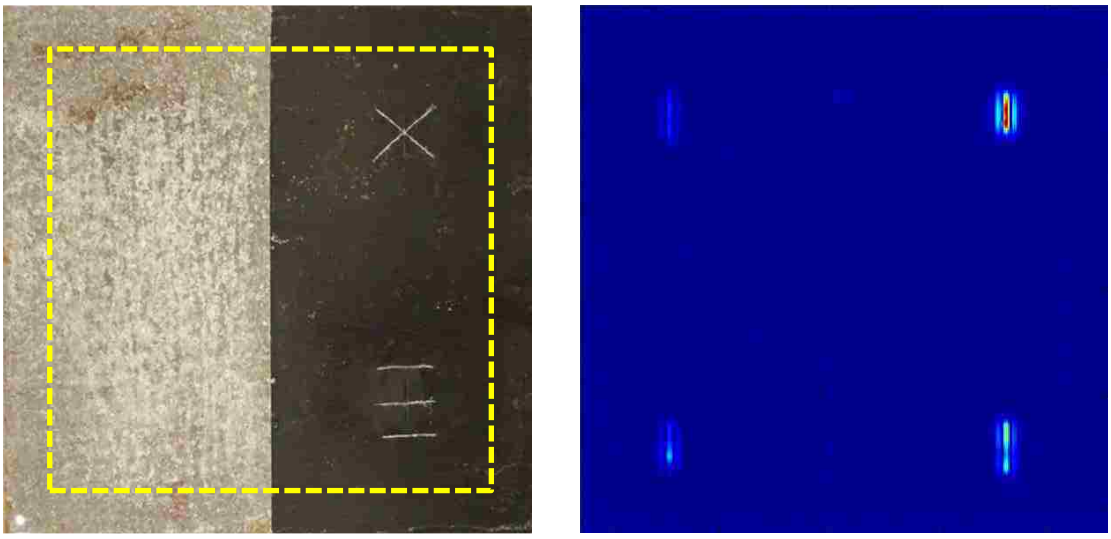

(a) (b)

Figure 3.24: (a) Sample 5 photograph after 72 hours in the salt-fog chamber with marked scan area and (b) SAR image of scan area.

The final SAR image, shown in Figure 3.26 (b), was obtained after 144 hours in the salt-fog chamber. Much like the previous cycles, all four cracks are still detected, although the overall intensity of the background due to corrosion/salt layer has slightly increased. The photograph of the sample at this time is shown in Figure 3.26 (a). Additional corrosion can be seen along the edges of the paint coating and around the slashes. The total thickness of the corrosion and salt layer was measured to be ~0.3 mm on the bare side of the sample.

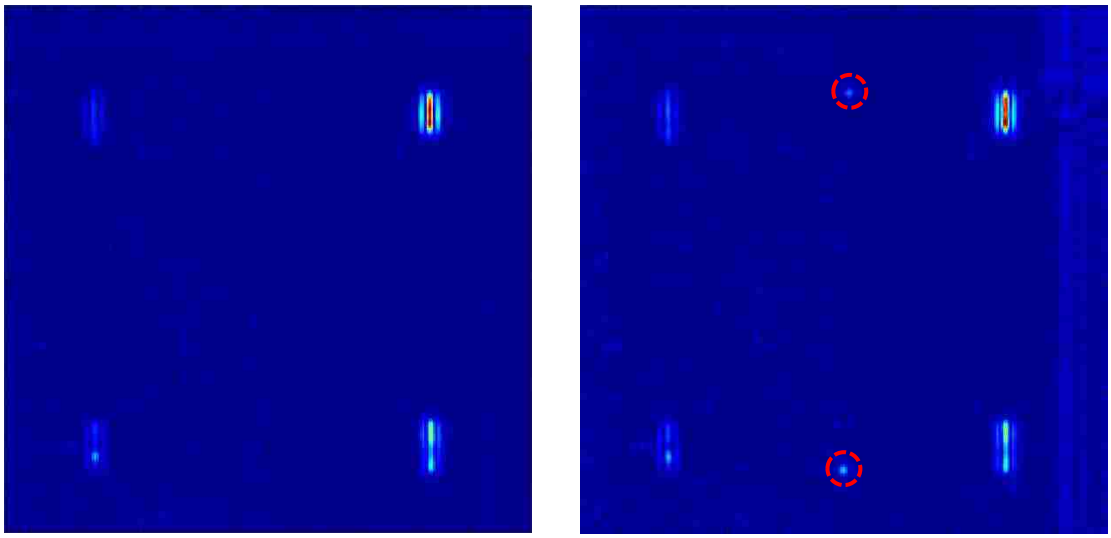

(a) (b)

Figure 3.25: Sample 5 SAR image after (a) 96 hours and (b) 120 hours in the salt-fog chamber.

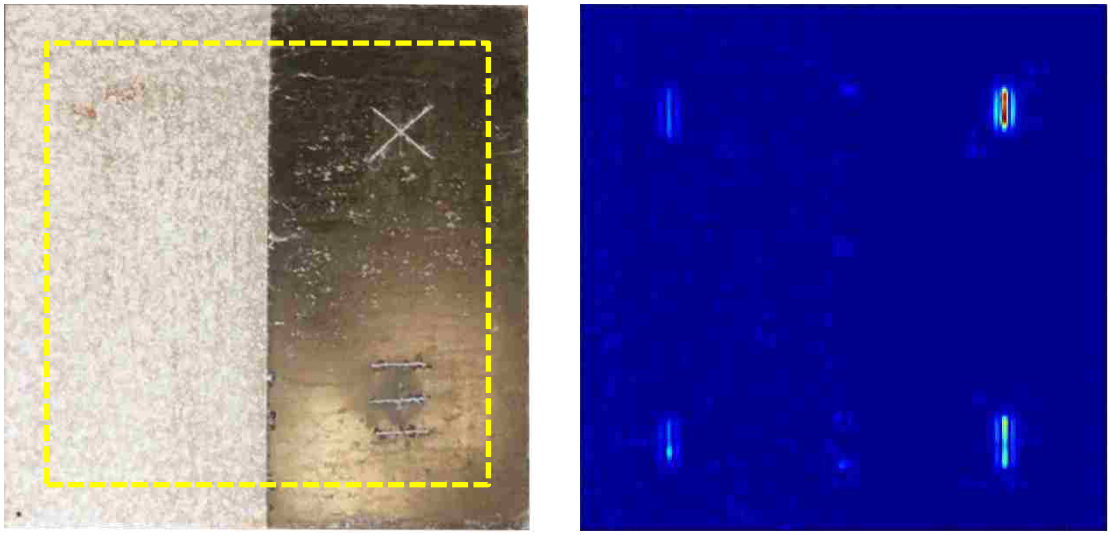

(a) (b)

Figure 3.26: (a) Sample 5 photograph after 144 hours in the salt-fog chamber with marked scan area and (b) SAR image of scan area.

3.6. SAMPLE 6: SAR IMAGES AT W-BAND (75 – 110 GHZ)

The final sample, sample 6, was a steel plate with two fatigue cracks. The sample is shown in Figure 3.27 (a). A close-up image of the crack is shown in Figure 3.27 (b).

The corresponding SAR image is shown in 3.28. Unlike the notches that were imaged on samples 1 – 5 this crack is extremely narrow making it much more difficult to detect. Figure 3.28 shows an indication of a crack. However, the difference between the intensity of the background and the crack is much lower than the 0-hour images from the other samples. This difference normally decreases as the thickness of corrosion increases, resulting in the crack to be undetectable much sooner than those in the other samples. Unlike the other cracks which were created artificially the crack on sample 6 has a slight surface level variation on each side of the crack, which makes the crack easier to detect as the different surface levels have a higher or lower image intensity. The following sample 6 SAR images are generated using a greyscale map instead of jet (red to blue) colormap as the cracks were more easily seen in this presentation format.

(a)

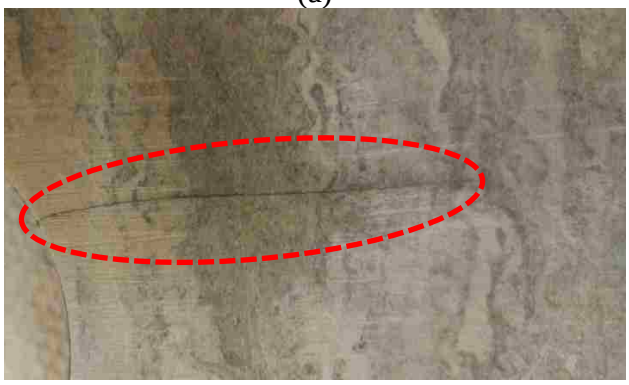

(b)

Figure 3.27: (a) Sample 6 photograph (b) close-up of crack.

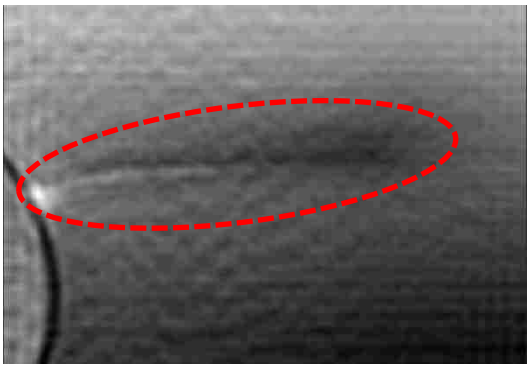

Figure 3.28: Sample 6 SAR image prior to corrosion.

After 24 hours in the salt-fog chamber, the sample was imaged again, as shown in Figure 3.29. The difference in the surface level on each side of the crack is not as prominent in this image making the indication less clear than the 0-hour image. The corrosion has very little effect on the image, but small splotches can be seen where corrosion is beginning to collect. In real world applications, locating the end of a crack is pivotal as it allows an operator to inhibit progression of a crack. However, in the 24-hour image the crack appears much shorter than it does in the 0-hour image. Although this method cannot exactly determine the end of the crack, it can be used to determine if there is a crack is present before surface preparation or further inspection is required.

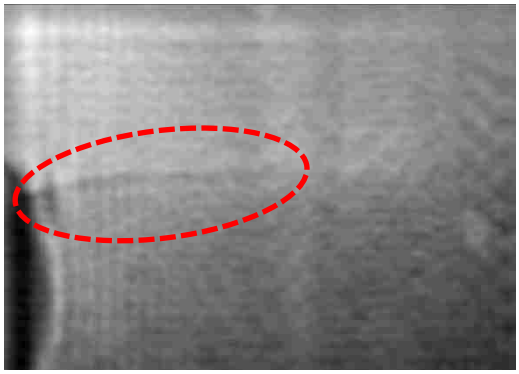

Figure 3.29: Sample 6 SAR image after 24 hours in the salt-fog chamber.

The final SAR image was made after 48 hours in the salt-fog chamber. Similar to the steel samples 1, 3, and 4, the corrosion increased after each 24 hour period in the salt-fog chamber, with obvious corrosion after just 24 hours. This time the SAR image, shown in Figure 3.30, shows clear signs of corrosion. Small pits and areas of higher density corrosion are well defined, while the crack is faintly seen. Determining what is or is not a crack at this time would heavily depend on the ability and experience of the operator. Having the knowledge of where cracks form and how they progress will be benficial when discriminating between corrosion, cracks and image anomalies. Consequently fatigue cracks usually form from the edge of a material and as shown in Figure 3.30, circled in red, a small crack can be seen coming from the center hole. The total length of this indication has decreased after each 24-hour period in the salt-fog chamber.

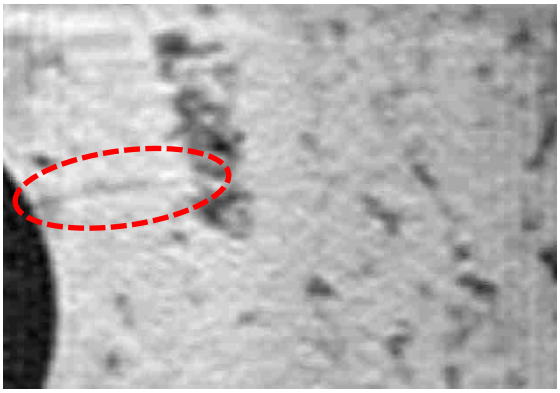

Figure 3.30: Sample 6 SAR image after 48 hours in the salt-fog chamber.

3.7. OVERVIEW OF RESULTS

Looking at the study as a whole we can arrive at certain conclusions. The ability to detect surface-breaking cracks dramatically decreases as the thickness of corrosion increases, as expected. Corrosion absorbs and scatters a millimeter wave signal. Metals that resist corrosion or that have a corrosion resistant coating provide favorable conditions for detecting cracks. As the corrosion builds up on the surface of a sample the image intensity of the "background" (the portion of the image that does not have a crack) increases. Thus, cracks are only distinguishable if there is a contrast between the crack image intensity and the background intensity. The cracks on the bare steel samples, samples 1, 3, and 4, were detectable up to 96 hours in the salt-fog chamber (or ~0.6 mm of corrosion). Microscope photographs of sample 3 are shown in Figure 3.31 (a - c) as examples of the severity of the corrosion and the condition of the sample after 144 hours in the salt-fog chamber.

The ability to distinguish a crack from the background can be quantified by the ratio of the mean (1) of the amplitude of the crack to the variance (2) of the "background"; we call this quantity signal-to-noise ratio (SNR) [32]. The mean value of the crack, μ_{crack}, is the summation of the pixel values (s_i) that are in the region around the crack, divided by the number of pixels. The squared variance of the background, σ_{bg}^2, is the summation of the difference between each pixel and the mean of the entire "background" area, $\overline{bg}$, squared, divided by the number of pixels minus one. Equation (3), which shows the expression for SNR in dB is used in [32] to describe SNR in images. Analysis using this approach was used to develop a metric associated with the ability to detect cracks under certain conditions. The two bare samples, sample 1 and 2,

were analyzed to show the difference between crack indications on corrosion prone and corrosion resistant metals. Additional analysis was performed on sample 3 to illustrate how indications under corrosion resistant coating could be detected after much more time in the salt-fog chamber than bare metal.

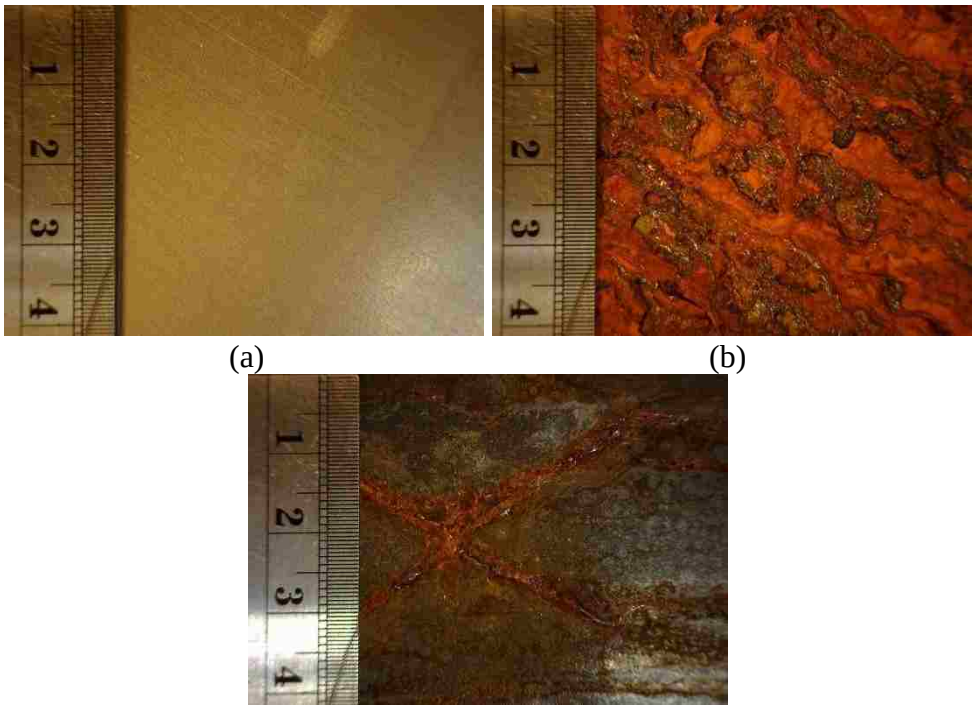

(a) (b)

(c)

Figure 3.31: Photos of (a) the bare portion of sample 3 prior to weathering, (b) the bare portion of sample 3 after 144 hours in the salt-fog chamber, and (c) the crack and slashes found on the painted half of region A of sample 3.

$$\mu_{crack} = \frac{1}{N}\sum_{i=1}^{N} s_i \tag{1}$$

$$\sigma_{bg}^2 = \frac{1}{N-1}\sum_{i=1}^{N}\left(bg_i - \overline{bg}\right)^2 \tag{2}$$

$$SNR(dB) = 20 * \log_{10}\left(\frac{\mu_{crack}}{\sigma_{bg}}\right) \tag{3}$$

The importance of analyzing the SNR associated with a crack indication in an image is to identify how much background variation can be tolerated before a crack is no longer detected. A threshold approach was implemented that determines if a crack is distinguishable from the background. The value selected for this threshold (13 dB), was determined based on the images of sample 1; 13 dB represents when the cracks were last detectable with a minimum amount of background clutter that could be misconstrued as cracks. This value is not absolute and should be further investigated to balance the probability of detection and false-positives. Figure 3.32 (a) shows the SNR for the two cracks highlighted in Figure 3.32 (b) after each 24-hour period in the salt-fog chamber.

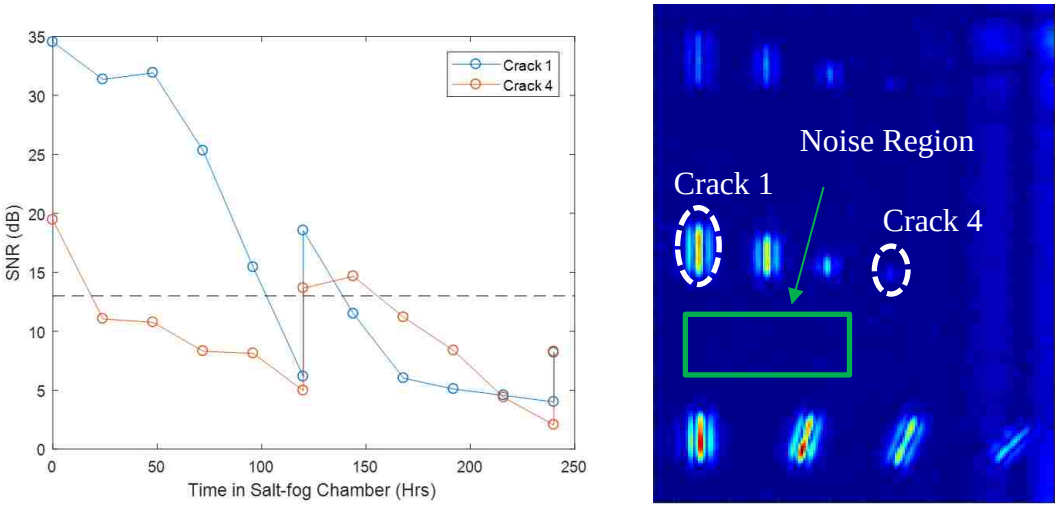

(a) (b)

Figure 3.32: (a) SNR of the SAR indications of (b) reference for cracks 1 and 4 (region B of sample 1) and respective noise region.

The SNR of the cracks on the steel samples constantly degraded as the amount of corrosion increased. When the SNR dropped below the detection threshold, (i.e. there were no crack indications) the excess corrosion was removed. This process was done at

120 and 240 hours, which is the reason for the two data points at those times. In each case, this improved the overall quality of the SAR image. The improvement was large enough for the 120-hour image so that the indications of the cracks were again distinguishable from the background. However, as corrosion thickness increased, the removal of excess corrosion did not help much in detecting the crack after additional periods of corrosion inducing exposures. This is evident in the 240-hour image, which showed some improvement as crack indications could be seen but were difficult to distinguish from the background. The trend of decreasing SNR of the crack indications, with increasing thickness of corrosion, was apparent for all the bare or partially bare steel samples, samples 1, 3, 4, and 6.

The results of the aluminum samples, samples 2 and 5, followed a considerably different trend. As the time in the salt-fog chamber increased, the SNR of the cracks on the samples never fell below the detection threshold, as shown in Figure 3.33 (a). Unlike the steel samples that continuously corroded, the aluminum samples formed a thin layer of aluminum oxide (the corrosion byproduct of aluminum) that prohibited further corrosion. After 72 hours in the salt-fog chamber, the sample's surface was no longer cleaned after each period in the chamber. As the thickness of the salt deposits increased, the intensity of the background variation in the SAR images also increased, thus decreasing the SNR of the cracks. Cleaning the samples prior to the 240-hour measurement increased the overall SNR of the cracks. This may be relevant in cases of extreme salt build up on ships or bridges that need to be inspected near saltwater bodies.

The results of the SAR images taken of the samples with corrosion resistant paints on a portion of the sample, samples 3-5, were relatively similar to each other. The SNR

over time in the salt-fog chamber for two of the cracks on sample 3 is shown in Figure 3.34 (a). Cracks 1 and 2, highlighted in Figure 3.34 (b), were selected to show the difference between a covered and uncovered crack as the thickness of corrosion increases.

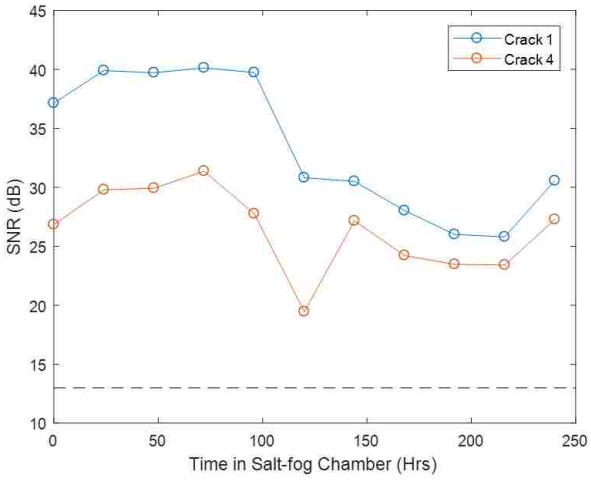

(a)

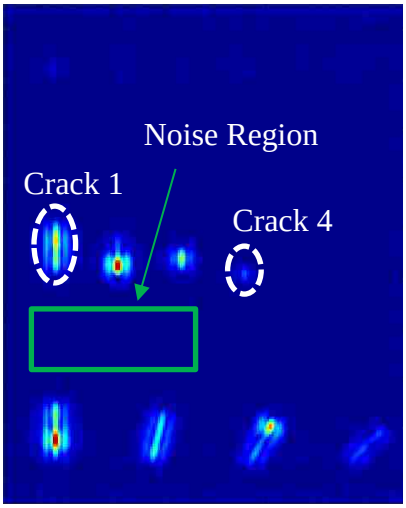

(b)

Figure 3.33: (a) SNR of the SAR indications of (b) reference for cracks 1 and 4 (region B of sample 2) and respective noise region.

When calculating the SNR for each crack, the noise region was selected from the half of the sample similar to where the crack was formed. The sudden drop in SNR at 24 hours is due to the increase in scan step size (from 2 mm to 3 mm), which caused additional background variation. This effect was removed by returning the scan step size to 2 mm for the rest of the images. As the thickness of corrosion around crack 1 increases, the SNR of crack 1 steadily decreases until the crack is no longer detected (below threshold), which is similar to the behavior of the SNR of the cracks on sample 1 (Figure 3.32 (a)). Crack 2, which was covered in paint and therefore protected from

corrosion, had a constant SNR as the amount of time in the chamber increased. Once the corrosion begins to penetrate the protective layer, most likely from the edges of the paint or the slashes over the cracks, the SNR will decrease until the crack is no longer detected.

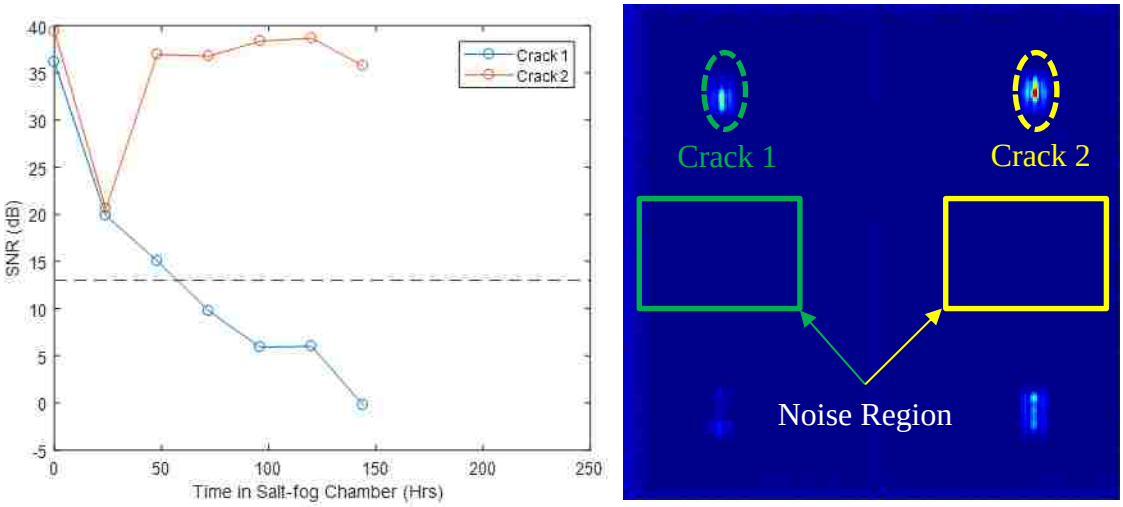

(a) (b)

Figure 3.34: (a) SNR of the SAR indications of (b) reference for cracks 1 and 2 (region A of sample 3) and respective noise region.

4. NUMERICAL SIMULATIONS

In addition to the experimental measurements, numerical simulations were performed to investigate the capability of microwave imaging to detect cracks under surface coatings (paint, primer, and corrosion). These simulations were performed using the EM full-wave simulation software CST Microwave Studio®. To reduce computational time linear scans were done when investigating the effect of crack width and depth on the SAR image across the crack. An example of the linear scanning procedure is shown in Figure 4.1. Similar to the experimental measurements one probe was used to measure the reflected signals from the samples. However, instead of moving the sample around the probe, the probe was moved around the simulation domain. The simulated images also have similar characteristics to the measurements, a step size between measurements of 2 mm and a standoff distance of 25 mm. Additional simulations were performed to investigate the effect of the length of a crack and the effect of surface coatings on top of a crack. These simulations featured two-dimensional scanning which is illustrated in Figure 4.2. All simulation data were subjected to the same processing as the experimental measurement data.

To reduce the overall computational time, simulations were limited to a single crack and a small imaging domain. Each simulation had an imaging domain of 30 mm x 30 mm, a step size of 2 mm and a standoff distance of 25 mm. The waveguide and the flange had identical dimensions to those used for the experimental measurements. The modelled crack dimensions and the surface coating of the metal were matched, as closely as possible, to the samples. The surface coatings were simplified to their base

components, primer to polyamide, paint to polyurethane, and corrosion to red rust. The dielectric constants of the paint (polyurethane ε_r = 3.55-j0.008) and primer (polyamide ε_r = 2.6-j0.001) layers were referenced from [33]. The measured dielectric constant of red rust, which was presented in Section 1.3.3 (ε_r = 8.7-j2.0) was used as well. Because the dielectric properties of each material were not measured at Ka-band (26.5 – 40 GHz), CST Microwave Studio® uses a built-in model to extrapolate the dielectric properties from known frequencies, the results of this extrapolation are shown in Figure 4.3. Prior to simulating cracks under corrosion, the effect of varying (increasing or decreasing from the starting values) the dimensions of cracks (i.e. length, width and depth) on the SAR image was investigated. During these analyses, the dimension being investigated was varied while the other dimensions were held constant (if investigating the effect of length, the width and depth were kept constant).

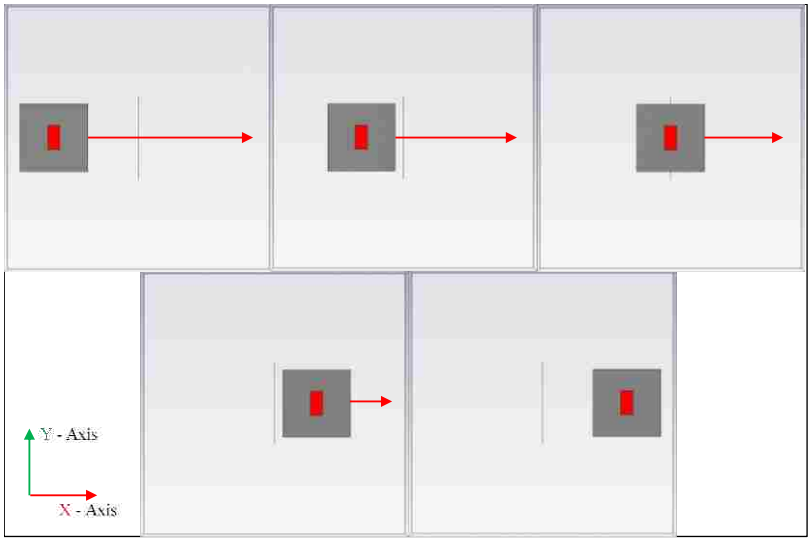

Figure 4.1: Top view of CST model, as a waveguide is scanned linearly across the crack (line scan).

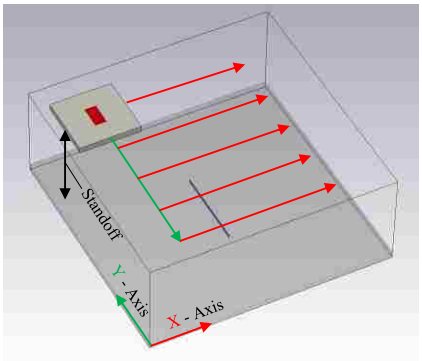

Figure 4.2: Orthographic view of CST model, as a waveguide is scanned in two dimensions over a crack (image scan).

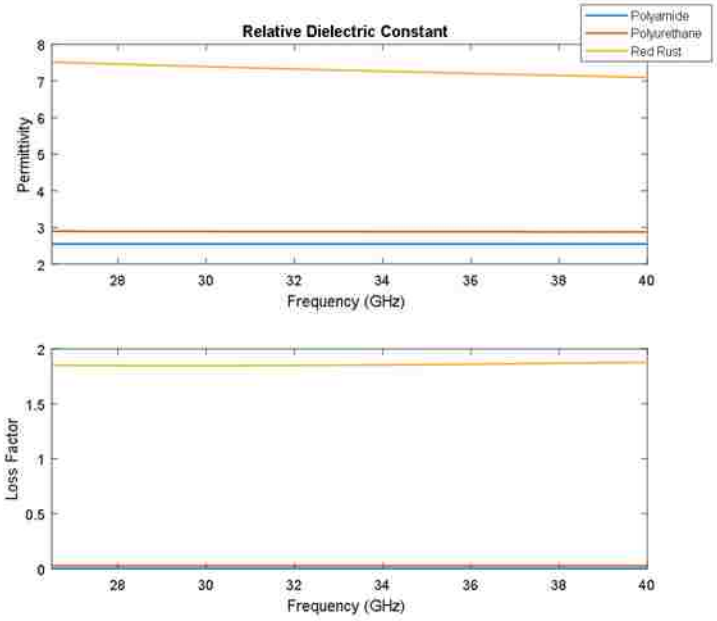

Figure 4.3: Dielectric constant of coatings used in numerical simulations.

4.1. CRACK RESPONSE VS. WIDTH

To investigate the effect of crack width on its SAR image a simple model of a crack on a plate was imaged. The width of the crack was varied from 0.1 mm to 1.0 mm and had a fixed length and depth of 25.4 mm and 1 mm, respectively. Just as the experimental measurements were made, albeit with only one scanning direction, as

shown in Figure 4.1, a waveguide was moved in fixed steps across the center of the crack. The reflected signal was measured at the waveguide as it would be if using a network analyzer (magnitude and phase at each frequency point). The resulting linear SAR data is shown in Figure 4.4, as the width of the crack increases the magnitude of the indication increases. Although the manufactured cracks were all made with the same saw, this data shows how cracks of various widths would show up in a SAR image. The manufactured cracks also fall within the lower magnitudes as their width was between 0.1 mm and 0.25 mm. While cracks of this size are detectable, the magnitude of the SAR image is quite low, and the effect of corrosion does not have to be that large to overpower the crack indication. Consequently, a slightly wider crack, which has a much stronger response, would be more easily detectable under further corrosion than the cracks used in this study.

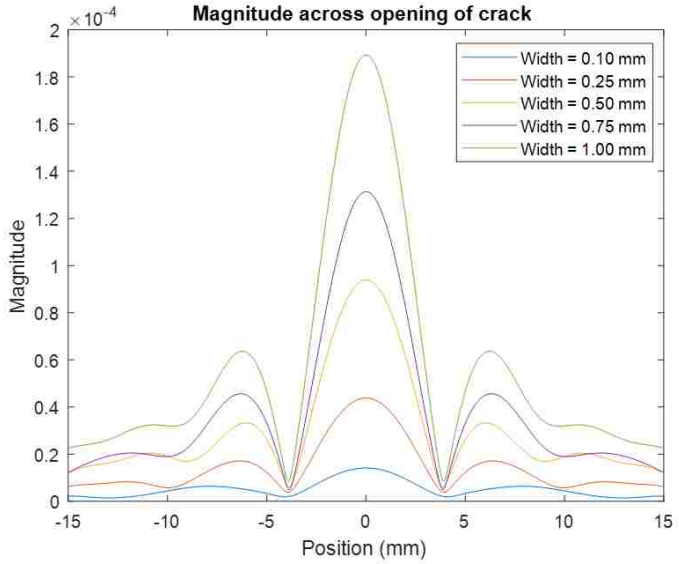

Figure 4.4: Magnitude of the SAR response focused at the distance of the crack as the width of the crack varies.

4.2. CRACK RESPONSE VS. DEPTH

For cracks that do not penetrate through the metal surface, the depth is an important characteristic that can limit the probability of detection. To illustrate the effect depth has on the magnitude of the SAR image, the depth was varied from 0.25 mm to 1.5 mm, while the width and length were fixed, at 0.1 mm and 25.4 mm, respectively. Similar to the analysis on the effect of the crack width on the SAR image, linear scans were performed to reduce computational time while still obtaining sufficient information. Figure 4.5 shows the magnitude of the SAR image across the width of the crack. Unlike the crack width, there is not a direct relationship between the magnitude of the SAR data and the depth of the crack. However, the relationship between depth and magnitude is monotonic (increasing depth increases magnitude of SAR image). When the crack does not fully propagate to the other side of the metal the crack acts as a cavity, making the response a function of frequency and the dimensions of the crack, this was detailed in [13]. As a result, the intensity of the crack indication oscillates with an overall increasing trend as shown in Figure 4.5 [13]. The manufactured cracks in this study targeted a depth of 0.25 mm and 0.5 mm. Cracks of around this depth appear very similar in simulation but appeared much different in measurements, with the cracks of depth ~0.5 mm appearing much stronger than the cracks with a depth of ~0.25 mm. This is most likely due to the cracks being on average deeper than desired, as they were hand cut. Slight changes in depth can have a larger impact than others, as shown in the jump in magnitude from the depth of 1 mm to the depth of 1.25 mm, in Figure 4.5. It would have beneficial to increase the desired depth as the response was much stronger, which could have been detected under thicker corrosion.

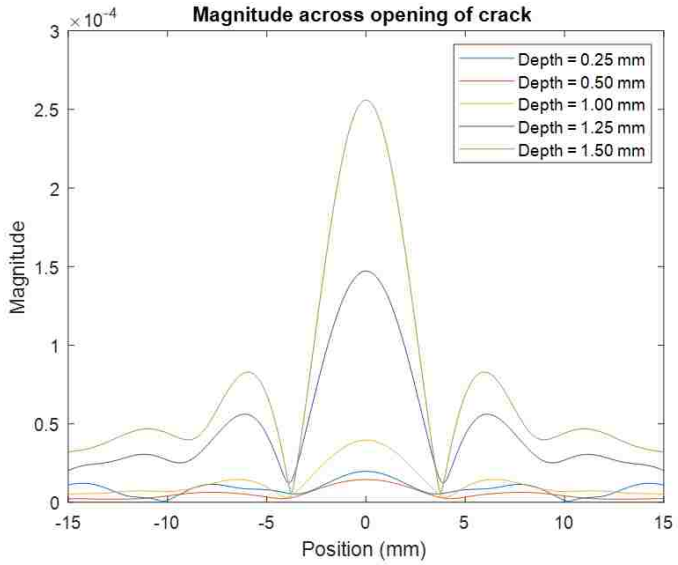

Figure 4.5: Magnitude of the SAR response focused at the distance of the crack as the depth of the crack varies.

4.3. CRACK RESPONSE VS. LENGTH

While changing the width and depth of a crack greatly changes the possibility of detection, the effect of the crack length on SAR image is not as great once the crack reaches a certain size. Similar to the other investigations, the length of the crack was varied from 6.35 mm to 25.4 mm, while the width and depth was fixed at 0.1 mm and 1 mm, respectively. Unlike the width and depth investigations, linear scans across the crack do not provide sufficient information to determine the effect of the length of the crack on the SAR image. Instead, images were made, the imaging process was as shown in Figure 4.2. The resulting SAR images are shown in Figure 4.6. These images show as the length of the crack increases the overall intensity does not increase after the crack reaches a certain electrical length, as the 12.7 mm long crack and the 25.4 mm long crack have the same maximum intensity. The center frequency of the band has a wavelength of ~9 mm, which coincides with a crack length between the two shorter cracks. After this point the

intensity associated with the crack does not increase any longer. These simulations closely match the measurement results of the cracks in region A of Sample 1, which are shown in Figure 4.7. Small variations between the simulation and the measurements are due to the slight imperfections in the manufactured cracks (i.e. different width and/or depth between the cracks).

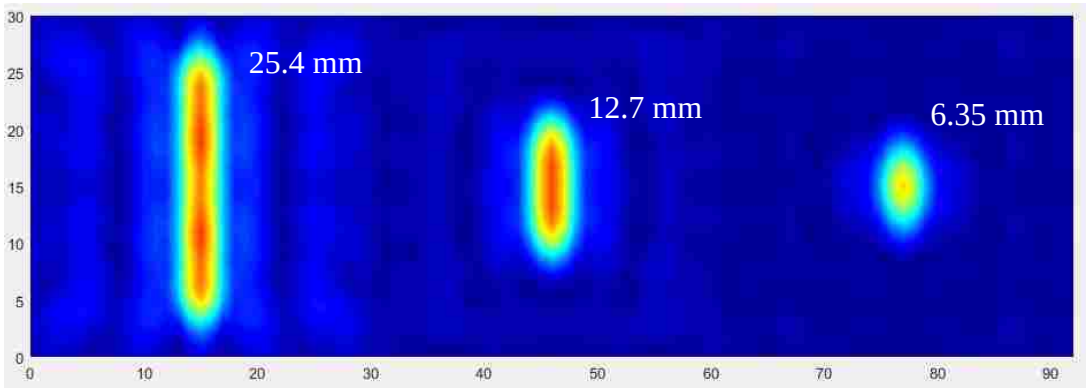

Figure 4.6: SAR image of simulated cracks, length from left to right: 25.4 mm, 12.7 mm, and 6.35 mm.

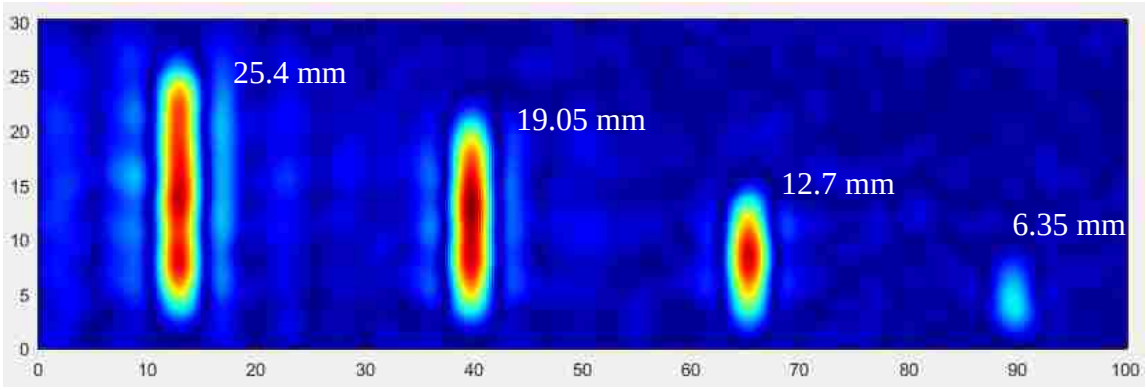

Figure 4.7: SAR image of experimental cracks from sample 1 region A, length from left to right: 25.4 mm, 19.05 mm, 12.7 mm, and 6.35 mm.

4.4. CRACK RESPONSE VS. CORROSION THICKNESS

Further simulations were conducted to determine the theoretical response of a crack with a corrosion byproduct coating. The thickness of the corrosion layer was selected from a linear fit of the previously measured data on the bare side of sample 3, as shown in Figure 4.8. The thicknesses were selected to be 0, 0.125, 0.25, and 0.375 mm corresponding closely to the corrosion thickness at 0, 24, 48, and 72 hours, respectively. The corrosion layer (red rust) was modelled on the surface of the sample; part of the corrosion layer replaced the metal on the surface to represent metal loss. Two similar simulation domains were created. Both included a crack with a length of 25.4 mm, a width of 0.1 mm, and a depth of 1 mm. One had a corrosion resistant coating with a thickness of 0.25 mm, while the other was left bare. The coating was divided into two equal thickness of paint and primer, with the paint layer being on top of the primer layer, the dielectric properties of both were shown in Figure 4.3.

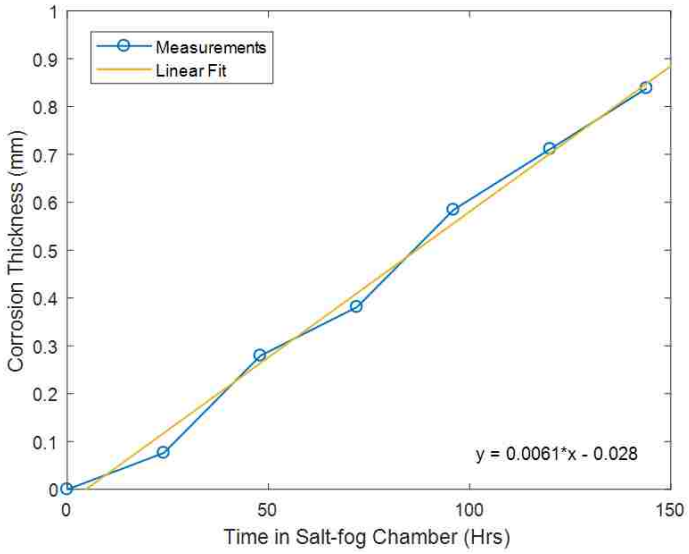

Figure 4.8: Thickness measurements of corrosion on sample 3 over time in the salt-fog chamber and corresponding linear fit.

The resulting SAR images of these two simulations are shown in Figures 4.9 and 4.10, respectively and the images are scaled to each other (similar colors represent similar intensity). The image of the bare cracks in Figure 4.9 shows the decrease in intensity of the crack as the thickness of corrosion increases, which is expected, as there is more loss as the thickness increases. The image of the paint-covered cracks in Figure 4.10 shows a similar decreasing trend in intensity as the corrosion thickness increases. However, Figure 4.10 also shows improved focusing of the crack indication, compared to Figure 4.9, when there is an additional dielectric layer (paint and primer) above the corrosion layer, this improvement was also shown in [34]. For these simulations, it was assumed that the coating layer was intact, but corrosion formed between the metal layer and the coating. While this did not happen as severely for the real samples this shows the worst-case scenario. As expected, as the thickness of corrosion increases the amount of signal returning from the crack decreases and the indication becomes fainter. However, these simulations also assume that the corrosion layer is uniform in thickness and dielectric property across the sample. In practice, corrosion is non-uniform and as such, large changes in surface variation can mask indications of the cracks, making real world cracks much more difficult to detect. Regardless, these simulations show that the crack indications become much weaker under increasingly thick corrosion and will soon be undetectable. This timeline coincides with the inability to detect cracks after the samples had been in the salt-fog chamber for 96 hours in the experimental measurements.

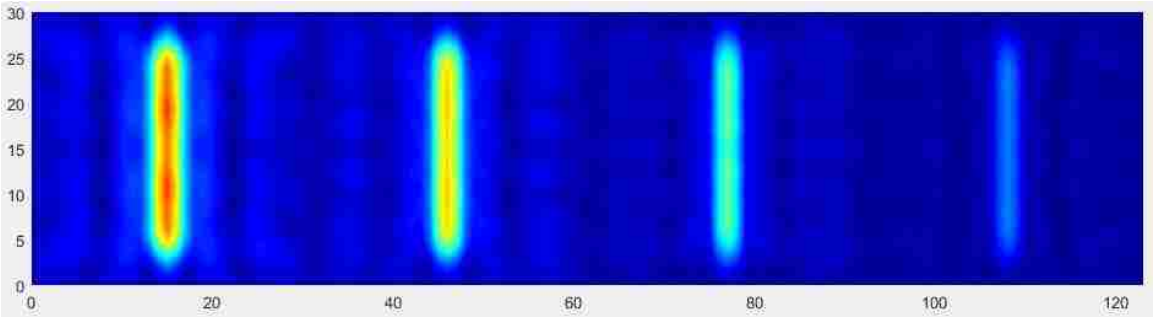

Figure 4.9: Uncovered cracks, from left to right: 0, 0.125, 0.25, and 0.375 mm of corrosion (Red Rust).

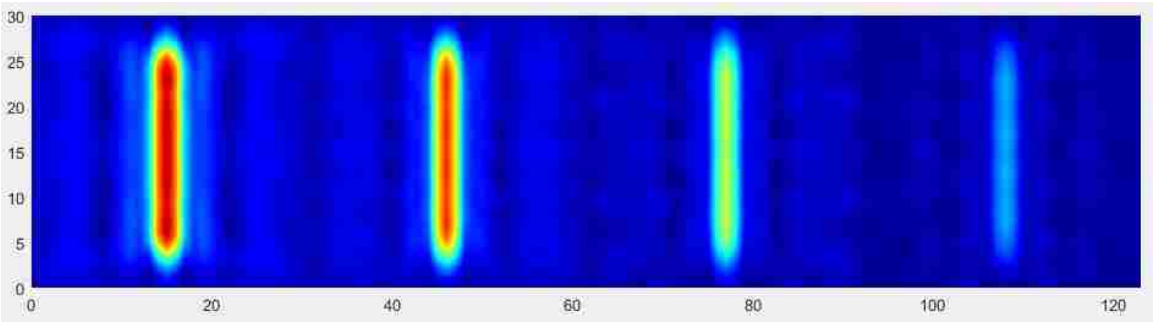

Figure 4.10: Cracks with a 0.25 mm thick paint and primer coating, from left to right: 0, 0.125, 0.25, and 0.375 mm of corrosion (Red Rust).

5. FINAL THOUGHTS

5.1. CONCLUSIONS

Detecting surface breaking cracks in metal structures under heavy corrosion is a very difficult task. This research proposes a technique that utilizes microwave and millimeter wave SAR imaging to detect cracks under surface coatings, such as heavy corrosion and/or paint) and identify key characteristics of the crack such as size and orientation. The main limitation of current techniques is the ability to detect cracks on unclean or uneven surfaces. This study illustrated the capability of microwave SAR imaging to detect cracks on two main types of structural metals, steel and aluminum. Each of the six samples were placed in a salt-fog chamber for 24-hour intervals until the cracks were no longer detected. Some of the samples were coated in a corrosion resistant paint or primer to evaluate if the method could also be used for detecting cracks under coatings that had been compromised by corrosion.

A standard linear-polarized, rectangular waveguide probe was used to image samples 1 – 5 at Ka-band (26.5 – 40 GHz), and sample 6 at W-band (75 – 110 GHz). The resulting images were visually examined for crack indications and a detection metric (referred to as SNR), based on the relative strength of the indication compared to the background variance of the image, was derived. This metric showed that as the thickness of surface coating (corrosion or salt deposit) increased, the SNR of the crack indication decreased. When the SNR of a crack indication fell below a certain threshold (defined empirically at 13 dB, as the point where the indication could be misconstrued as background variation) the crack was classified as undetected. This point occurred

between 72 and 96 hours in the salt-fog chamber for most of the cracks on the steel samples and did not occur for the aluminum samples. Shallower cracks were the first to go undetected, with the length of the cracks being a smaller factor of detectability (if cracks are of sufficient length).

Numerical simulations were also conducted to verify the capability of this method. Simulated cracks, with similar dimensions to that of the experimental samples, were imaged at Ka-band (26.5 – 40 GHz) in a same manner as the experimental measurements. A thin layer of corrosion was modelled on the surface, with a thickness of approximately the measured thickness of corrosion on sample 1 after 24, 48, and 72 hours in the salt-fog chamber, 0.125, 0.25, and 0.375 mm, respectively. The simulated images showed that the loss from the corrosion layer makes crack indications weaker as the thickness of corrosion increases until a point that the cracks are no longer seen. This occurs after the corrosion thickness exceeded 0.375 mm if all parameters of the corrosion (i.e., thickness and dielectric properties of the corrosion) are uniform throughout. Furthermore, the simulations showed that having a thin low loss dielectric layer (in this case paint) above the corrosion improved focusing capability, making the intensity of the indication stronger; this was previously shown in [34].

5.2. LIMITATIONS

Although microwave and millimeter wave SAR imaging offers alternative benefits that current methods do not provide, it does not come without its own limitations. While microwaves can readily penetrate many materials, their interaction with the material is significant. In this study steel corrosion, or red rust, presented the

biggest limitation to this method. The dielectric losses of red rust are high; the loss tangent is about 0.25 at X-band (8.2 – 12.4 GHz), compared to that of NaCl and corrosion resistant coatings (polyurethane or polyamide) where the loss tangent is ~0.005. This loss was shown, in simulation and measurement, to reduce the overall intensity of crack indications as the thickness of corrosion increases. Once the returning signal becomes too small the crack is no longer be detectable. In the experimental measurements this point occurred after 72 hours in the salt-fog chamber, which resulted in a corrosion thickness of 0.375 mm. The effect of this issue could be reduced if the system was optimized for penetrating red rust corrosion, such as selecting a frequency band that has less loss through the corrosion, or a frequency band that interacts more strongly with the crack, in turn increasing the intensity of the crack indication. Another limitation of microwave and millimeter wave SAR imaging is the frequency dependence on detecting small cracks. At Ka-band (26.5 – 40 GHz) cracks with a width above 0.1 mm are detectable, albeit under less corrosion as the intensity of the SAR image of a crack this small is very low. As the dimensions of the crack get smaller higher frequencies are needed for detecting them. Currently, as frequency increases hardware costs greatly increase, this could be resolved with time as hardware prices decrease. In the end, setting a size and surface condition threshold will be an important part of determining the limits of each system.

5.3. FUTURE WORK

While this study illustrated a capable method for detecting cracks, further analysis may provide additional benefits of the technique. Further capability could be possible at different frequency bands or with circularly polarized probes. Investigating different

frequency bands, at either, lower frequency to improve dielectric penetration (lower losses), or higher frequency to improve crack detection capability (higher resolution and larger interaction with crack opening), could cater microwave or millimeter wave imaging to a specific application.

BIBLIOGRAPHY

[1] "Corrosion Costs and Preventative Strategies in the United States," https://www.nace.org/uploadedFiles/Publications/ccsupp.pdf., August 2018.

[2] "DoD Estimates the Annual Cost of Corrosion for Navy Ships," http://corrdefense.nace.org/corrdefense_fall_2012/DoD_1.asp. August 2018.

[3] "Highway Bridge Inspections," https://www.transportation.gov/content/highway-bridge-inspections. August 2018.

[4] "Nondestructive Evaluation and Structural Health Monitoring," https://highways.dot.gov/bridges-and-structure/long-term-bridge-performance/nondestructive-evaluation-and-structural-health. August 2018.

[5] "Application of Magnetic Particle Inspection in the Field of the Automotive Industry," https://www.ndt.net/article/ecndt2006/doc/Th.1.6.3.pdf. September 2018.

[6] "The A, C and D of aircraft maintenance," https://www.qantasnewsroom.com.au/roo-tales/the-a-c-and-d-of-aircraft-maintenance/., August 2018.

[7] "Aircraft Wheel and Fuselage Testing with Eddy Current and SQUID," https://www.ndt.net/article/ecndt98/aero/043/043.htm. August 2018.

[8] "NDT Method Summary," https://www.nde-ed.org/GeneralResources/MethodSummary/MethodSummary.htm., August 2018.

[9] "Eddy current imaging using array probes," https://www.ndt.net/events/ECNDT2014/app/content/Paper/239_Mook.pdf. August 2018.

[10] "Review of Literature on Probability of Detection for Liquid Penetrant Nondestructive Testing," https://pdfs.semanticscholar.org/f8a6/ae319ec25983e7405ef092f3cc2355ae8a11.pdf, August 2018.

[11] "Review of Literature on Probability of Detection for Magnetic Particle Nondestructive Testing," https://www.dst.defence.gov.au/sites/default/files/publications/documents/DSTO-TR-2794.pdf. September 2018.

[12] Zoughi, Reza. "Microwave and Millimeter Wave Nondestructive Testing Principles." *Materials Evaluation* 76.8 (2018): 1063-1069.

[13] Yeh, Chin-Yung, and Reza Zoughi. "A novel microwave method for detection of long surface cracks in metals." IEEE *Transactions on Instrumentation and Measurement* 43.5 (1994): 719-725.

[14] Kharkovsky, Sergey, Mohammad T. Ghasr, and Reza Zoughi. "Near-field millimeter-wave imaging of exposed and covered fatigue cracks." *IEEE Transactions on Instrumentation and Measurement* 58.7 (2009): 2367-2370.

[15] Ramzi, Mohammad R., et al. "Near-field microwave imaging using open-ended circular waveguides." *Imaging Systems and Techniques (IST), 2016 IEEE International Conference* on. IEEE, 2016.

[16] Yang, Seung-Hwan, Ki-Bok Kim, and Jin-Seob Kang. "Detection of surface crack in film-coated metals using an open-ended coaxial line sensor and dual microwave frequencies." *NDT & E International* 54 (2013): 91-95.

[17] Ghasr, Mohammad Tayeb, et al. "Comparison of near-field millimeter-wave probes for detecting corrosion precursor pitting under paint." *IEEE Transactions on Instrumentation and Measurement* 54.4 (2005): 1497-1504.

[18] Qaddoumi, Nasser N., Wael M. Saleh, and Mohamed Abou-Khousa. "Innovative near-field microwave nondestructive testing of corroded metallic structures utilizing open-ended rectangular waveguide probes." *IEEE Transactions on Instrumentation and Measurement* 56.5 (2007): 1961-1966.

[19] Case, Joseph T., Mohammad Tayeb Ghasr, and Reza Zoughi. "Optimum two-dimensional uniform spatial sampling for microwave SAR-based NDE imaging systems." *IEEE Transactions on Instrumentation and Measurement 60*.12 (2011): 3806-3815.

[20] Ulaby, Fawwaz Tayssir, et al. *Microwave radar and radiometric remote sensing*. Vol. 4. No. 5. Ann Arbor: University of Michigan Press, 2014.

[21] Ghasr, Mohammad Tayeb, et al. "Millimeter-wave differential probe for nondestructive detection of corrosion precursor pitting." *IEEE Transactions on Instrumentation and Measurement* 55.5 (2006): 1620-1627.

[22] Ghasr, Mohammad Tayeb, Kuang P. Ying, and Reza Zoughi. "SAR imaging for inspection of metallic surfaces at millimeter wave frequencies." *Instrumentation and Measurement Technology Conference (I2MTC) Proceedings, 2014 IEEE International*. IEEE, 2014.

[23] Gallion, John R., and Reza Zoughi. "Millimeter-Wave Imaging of Surface-Breaking Cracks in Steel With Severe Surface Corrosion." *IEEE Transactions on Instrumentation and Measurement* 66.10 (2017): 2789-2791.

[24] N. N. Qaddoumi et al., "Microwave Corrosion Detection using Open Ended Rectangular Waveguide Sensors," *Materials Evaluation*, vol. 58, no. 2, pp. 178-184, American Society for Nondestructive Testing, Inc., Feb 2000.

[25] Bois, Karl J., et al. "Dielectric plug-loaded two-port transmission line measurement technique for dielectric property characterization of granular and liquid materials." *IEEE Transactions on Instrumentation and Measurement* 48.6 (1999): 1141-1148.

[26] Rytting, D. K. "An analysis of vector measurement accuracy enhancement techniques." (1982).

[27] Ghasr, Mohammad Tayeb, Kuang P. Ying, and Reza Zoughi. "Wideband millimeter wave interferrometer for high-resolution 3D SAR imaging." *Instrumentation and Measurement Technology Conference (I2MTC), 2015 IEEE International*. IEEE, 2015.

[28] Qaddoumi, N., et al. "Microwave detection of stress-induced fatigue cracks in steel and potential for crack opening determination." *Journal of Research in Nondestructive Evaluation* 12.2 (2000): 87-103.

[29] "Cyclic Corrosion Testers," https://www.q-lab.com/documents/public/6ed712e7-2980-4634-a529-38f0def75a7a.pdf?ReturnUrl=/resources/brochures.aspx., September 2018.

[30] "Standard Practice for Operating Salt Spray (Fog) Apparatus," https://compass.astm.org/EDIT/html_annot.cgi?B117+16., September 2018.

[31] "Corrosion of Aluminum and Aluminum Alloys," https://www.asminternational.org/documents/10192/3456792/06787G_Sample.pdf/c4151917-99fc-46e8-a310-d5578d0af160., October 2018.

[32] Bushberg, Jerrold T., and John M. Boone. *The essential physics of medical imaging*. Lippincott Williams & Wilkins, 2011.

[33] "Dielectric Constant, Strength, & Loss Tangent," http://www.rfcafe.com/references/electrical/dielectric-constants-strengths.htm, September 2018.

[34] Qaddoumi, Nasser, and Reza Zoughi. "Microwave detection of corrosion under paint and composite laminate coatings." *Nondestructive Evaluation of Aging Aircraft, Airports, and Aerospace Hardware*. Vol. 2945. International Society for Optics and Photonics, 1996.

VITA

John Robert Gallion was born in Saint Peters, Missouri. In May 2017, he received his B.S. in Electrical Engineering from the Missouri University of Science and Technology, Rolla, Missouri, USA. He assisted research endeavors at the *amntl* research laboratory from November 2015 until December 2018. In May 2019, he received his M.S. degree in Electrical Engineering from the Missouri University of Science and Technology, Rolla, Missouri, USA. He has published several conference and journal papers, one is listed with the references of this research. Others include research done on material characterization and microwave and millimeter wave SAR imaging.